POLITECNICO DI TORINO

Master Degree
in Mechanical Engineering

Master Degree thesis

Numerical Analysis of the Influence of Rotation on Aerodynamic Effects in Axial Turbine Cascades

Supervisor

Prof. Daniela Anna Misul

Prof. Simone Salvadori

Co-Supervisor

M. Sc. Marco Hahn

Candidate

Gennaro Desiderio

April 2022

Contents

Symbols

Symbol	Unit	Description
Latins symbols		
C	m	Chord
D	1/s	Strain rate
L	m	Characteristic lenght
P	m	Pitch
T	K	Temperature
T_s	N/m^2	Stress tensor
Tu		Turbulence intensity level
U_∞	m/s	Inifnite velocity
b	N	External forces
c	m/s	Absolute velocity
e	kgm^2/s^2	Internal energy
h	m	Height of blade
p	Pa	Pressure
p_t	Pa	Total Pressure
p^*		Adimensional pressure ratio
$q^{\cdot}$	W/m^2	Heat flux
r		Radial coordinate
t	s	Time
u	m/s	Streamwise velocity, axial velocity
$u_{\tau,air}$	m/s	Friction velocity
v	m/s	Tangential velocity
w	m/s	Radial velocity
y^+		Dimensionless wall distance
Greek symbols		
Δt	s	Time interval
δ	m	Boundary layer thickness
θ		Angular coordinate
μ	kg/(ms)	Dynamic viscosity
μ_t	kg/(ms)	Eddy viscosity
ν	m^2/s	Kinematic viscosity
ρ	kg/m^3	Density
τ_{ij}	N/m^2	Term of stress tensor
ω	rad/s	Rotational velocity

Abbreviations	
BSL	Menter Baseline Turbulence Model
CAD	Computer Aided Design
CFD	Computational Fluid Dynamics
CFL	Courant, Friedrich and Levy number
DNS	Direct Numerical Simulation
LES	Large Eddy Simulation
RANS	Reynolds Averaged Navier-Stokes
RPM	Revolutions Per Minute
SKE	Second Kinetic Energy
SSG	Speziale, Sarkar and Gatski
SST	Shear stress transport
	Turbine Inlet Temperature

Indices	
centr	Centrifugal
cor	Coriolis
down	Downstream
fict	Fictitious
in	Inlet
up	Upstream

Non-dimensional numbers	
CC	Coriolis-on-Centrifugal force ratio
C_{SKE}	Second Kinetic Energy coefficient
C_l	Lift coefficient
C_{pt}	Loss pressure coefficient
Re	Reynolds number
Re_{cr}	Critical Reynolds number

List of figures

List of tables

1 Introduction

Nowadays, energy is the main point of several world discussions and is fully examined about every aspect. World is experiencing an ecological transition, thanks to a new awareness about the nature and the planet. After the 2030 Agenda for Sustainable Development and different new laws, everyone is called to be more careful and smarter; in particular scientists can be part of this process discovering new ways to produce, store and carry energy and improving the current processes. Also recent news reports a certain effort among the greatest countries that are asked to contribute actively to the fight against the world pollution. Beyond the more sponsored technologies, projected to the future, increasing the efficiency of the systems used until now can have a big impact on the environment, decreasing the energy request. About this specific case, researches, studies and prototypes allow to produce knowledge for new products.

In the current case, this effort is spent for gas turbines, mostly for their capability to provide constantly electric energy without depending on weather and on other conditions. Multiple kinds of fuels, as natural gas, fuel oils, kerosene and synthetic fuels, are employed in gas turbines; on the other hand, various polluting products are expelled: carbon monoxide, nitrogen oxides, Particulate Matter, carbon dioxide, methane and nitrous oxide. For fighting climate change and global warming, on 12 May 2021, the European Commission adopted the EU Action Plan: "Towards a Zero Pollution for Air, Water and Soil", a document that includes also a reduction of air pollution (European Commission, 2021); moreover, according to a EU draft of 2020, to be classed as a sustainable investment – one that makes a “substantial” contribution to curbing climate change – gas power plants must not produce more than 100 grams of CO_2 equivalent per kilowatt hour. This target is really hard to accomplish, but every kind of improvement on current gas turbines is appreciated and useful.

In addition, gas turbines are used in the aeronautical transport, as part of aircraft motors, affecting the release of important quantity of polluting gases; according to an evaluation by Air Transport Action Group, the global aviation industry produces around 2% of all human-induced carbon dioxide emissions while aviation is responsible for 12% of CO_2 emissions from all transports sources, compared to 74% from road transport. Studying gas turbines and improving their construction and process can provide healthier implications.

The actions, which are performed on gas turbines to improve the efficiency, try to enhance the temperature of the inlet of the turbine and the pressure ratio. The first requirement is fulfilled with the development of new technology and materials, capable to deal with higher fusion temperature and harsh thermal loads. At the same time, cooling on these components is necessary to ensure a high efficiency without damaging or compromising the working cycle.

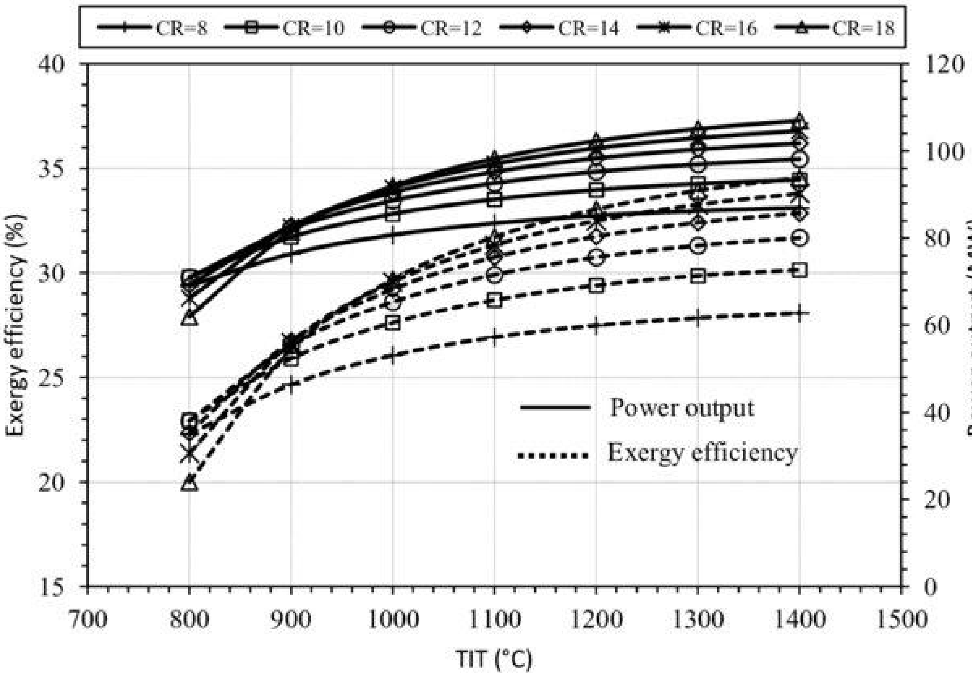

Figure 1.1 Effect of TIT and compression ratio on gas turbine power out and gas cycle exergy efficiency (Pattanayak, 2015)

Due to the large cost of production, different effects of a flow are studied thanks to simulations. Computational Fluid Dynamics (CFD) software enables realistic simulations for investigating every point about aerodynamics and thermodynamics; in this way, the flow is studied without the presence of the real component. Setting geometry, mesh and all the conditions, a system can be tested in first approximation fast and cheaply; several parameters can be combined for analyzing the different correlations and for publishing interesting outcomes.

Professor Lyczkowski (Lyczkowski, 2010) tells how CFD is developed during the years, valorising this technique and explaining how it can be considered a new science, with exciting applications as biological engineering. As Davidson declares (Davidson, 2002), CFD is routinely used today in a wide variety of disciplines and industries, including aerospace, automotive, power generation, chemical manufacturing, polymer processing, petroleum exploration, medical research, meteorology, and astrophysics. The use of CFD in the process industries has led to reductions in the cost of product and process development and optimization activities (by reducing down time), reduced the need for physical experimentation, shortened time to market, improved design reliability, increased conversions and yields, and facilitated the resolution of environmental, health, and right-to-operate issues. It follows that the economic benefit of using CFD has been substantial, although detailed economic analyses are rarely reported.

In conclusion, this kind of approach can help to improve the assemblies that produce energy, optimizing the process and reducing the pollutants, to accomplish to modern challenges: environment and energy.

1.1 Scope of research

In the research and development approach, prototypes allow to have a suitable reproduction of the product that is designed. In some cases, this kind of approach is not available due to technological, business or resource limits: exactly in this circumstance, simulations come into play and contribute to have a precise overview of a physical problem. The reduction of reality of the study is paid by the relative cheap cost of analyses and the ease of use of the software.

The importance of simulations has increased thanks to the improvements of the IT technology and the creation of new codes and algorithms that reduce time and complexity for studying a new product, keeping all the variables relevant.

About the studied topic, the project is followed by Institut für Thermische Strömungsmaschinen (ITS) of Karlsruher Institut für Technologie (KIT), in Karlsruhe, Germany. The experimental rig has been designed previously by the owner of the study - and co-supervisor of this thesis - to test the flow through a turbine cascade. Four airfoils with high stagger angle are arranged on a platform along a path characterized by a curve of 90 grades. The air flow is subjected to high deviation, creating consequently vortexes and turbulence effects. The experiment develops pushing a flow of air, controlled in terms of temperature and velocity profile, setting the outlet pressure. The future steps provide for the implementation of some cavities under the base, necessary for the practical construction of the prototype but relevant also for studying the thermal interaction of the flow with an underneath cooling flow.

This thesis wants to study the influence and the effects of the rotation on the prototype, to judge the eventual negligibility of this parameter; running the experiment in a static configuration, the effects of this variable cannot be observed. Implementation of rotation seems a hard task, considering the shape and the increment of budget. It is obvious that the model has to include the revolving action of the turbine rotor in a proper way, so applying a rotation on a linear platform is physically incoherent. For this reason, the CFD software is able to add and simulate the fictitious forces as Centrifugal and Coriolis force, keeping the planar configuration of the rig.

With this approach, a wider overview on the physical problem is possible; in fact, rotation could have a strong influence on the flow, about pressure, temperature and velocity.

Moreover, this condition is closer the real one of the working turbine, which can get very high number of RPM.
The knowledge provided by the thesis can give a prediction about the different working points of the turbine and it is a beginning point for the future thermal and heat transfer application. Studying secondary flow, vortexes and other parameters allows to improve the design and the process of the component. Understanding the aerodynamics of the flow helps for extreme working conditions and for setting the limits of the operation.
The main independent variable of this study is rotational velocity but also turbulence model and turbulence intensity can be set for plotting different results. Comparing with scientific literature and other qualitative experimental data, the study produces a powerful description of the flow. Although a complete substitution of the experiment is impossible, the aim is giving a great review of the rotation influence and providing the starting conditions and theoretical fundamentals for thermal analysis, describing a more complex and complete prototype. In conclusion, the thesis gives numerical correlations between the rotation and the aerodynamics effects.

1.2 State of research

Scientific community has worked considerably about turbine efficiency and working mode, examining in depth aerodynamics and thermal parameters. Starting from the aerodynamic field, secondary flow in turbomachinery has been highly analyzed, about different features and for several conditions.
Firstly, the scientific paper by Galina Ilieva (Ilieva, 2017) collects the different models presented along the time and establishes how the study could provide a better knowledge about the copious variables to consider. Previously, Langston published a review about the preceding 25 years studies (Langston, 2001), quoting the words of the past scientists of the topic and illustrating conventional parameters, as pressure loss coefficients, and original ones, as the parameter E, introduced by Eckerle and Awad and used for correlating their and others' data (Eckerle & Awad, 1991), or the quality factor Q (Weiss & Fottner, 1995). Secondary flow has been studied also linked to other quantities; in case of Mach number, the importance of secondary losses, compared to profile losses, is found to be diminishing as the Mach number rises (Perdichizzi, 1990) while load distribution affects the flow because the strong deflection, generates strong transverse pressure gradients that react on a relatively undisturbed thick boundary layer with high velocity gradients (Weiss & Fottner, 1995).
A little digression is soon made for presenting some parameters used in the last part of the thesis. Loss pressure coefficient C_{pt} was used during the processing of the experiment about a multistage radial inflow turbine (Li & Zheng, 2006); before Chaluvadi and his

colleagues (Chaluvadi, et al., 2001) adopted the same value to describe part of their results about the blade row interaction in a high pressure. It is computed as the double difference of total pressure between the inlet and the evaluated point divided by the product between the density ρ and the squared infinite velocity U_{∞}^{2}.

$$C_{pt} = \frac{p_{t,in} - p_{t,x}}{\frac{1}{2}\rho U_{\infty}^{2}} \tag{1.1}$$

The non-dimensional ratio allows to understand the load distribution along the channel and shows some similarities with the vorticity contours.
The second introduced coefficient is about the study of velocity field along the channel. Velocity, considered as vector with magnitude and direction, can provide information through the depiction of another dimensionless ratio. The SKE (Second Kinetic Energy) coefficient C_{SKE} was introduced by the team of the Department of Mechanical Engineering of United States Naval Academy in their paper for presenting some of their results about the secondary flow in a turbine passage (Aunapu, et al., 2000); the 3D plot shows on different planes how the turbulence – as deviation of free stream velocity – is present. Numerically, it is computed as:

$$C_{SKE} = \frac{v^{2} + w^{2}}{U_{\infty}^{2}} \tag{1.2}$$

Another aspect that has often been studied is the forces linked to the rotation. In particular, it has been stated that the combined effect of the Coriolis and centrifugal forces causes the separation near the leading surface and the acceleration of the flow near the trailing surface (Sleiti & Kapat, 2006). Closer to the aerodynamic application, a Coriolis-on-Centrifugal force ratio (1.3) was introduced to measure the weight of one force on the other one (Bangga, et al., 2017).

$$CC = \frac{\sqrt{\left(Cor_{y}^{2} + Cor_{z}^{2}\right)}}{F_{centr}} \tag{1.3}$$

A series of different measurements in different conditions have been taken over the years: introduction of a fence in the middle of the channel (Moon & Koh, 2000), in linear turbine cascade (Wang, et al., 1997), in multistage axial turbine (Porreca, et al., 2007), or in a shrouded axial turbine (Schlienger, et al., 2005). They generally show that the measurements reveal an interesting mechanism between the passage vortex and the wake.

It is usually rolled up into the secondary flow vortical system at the rotor hub, as a result of the induced secondary velocity field of the passage vortex.

About the replication of the rotation effects on planar turbine cascade, in 1992 a rotative adaption of a cascade was designed (Yaras & Sjolander, 1992). Thanks to the project by Danias of 1987 in Figure 1.2, Yaras and Solander tried to reproduce phisically rotation on a turbine cascade for studying the tip leakage. They concluded that the passage vortex was enhanced by the scraping effect of the blades and vortices were dragged toward the suction side of the passage.

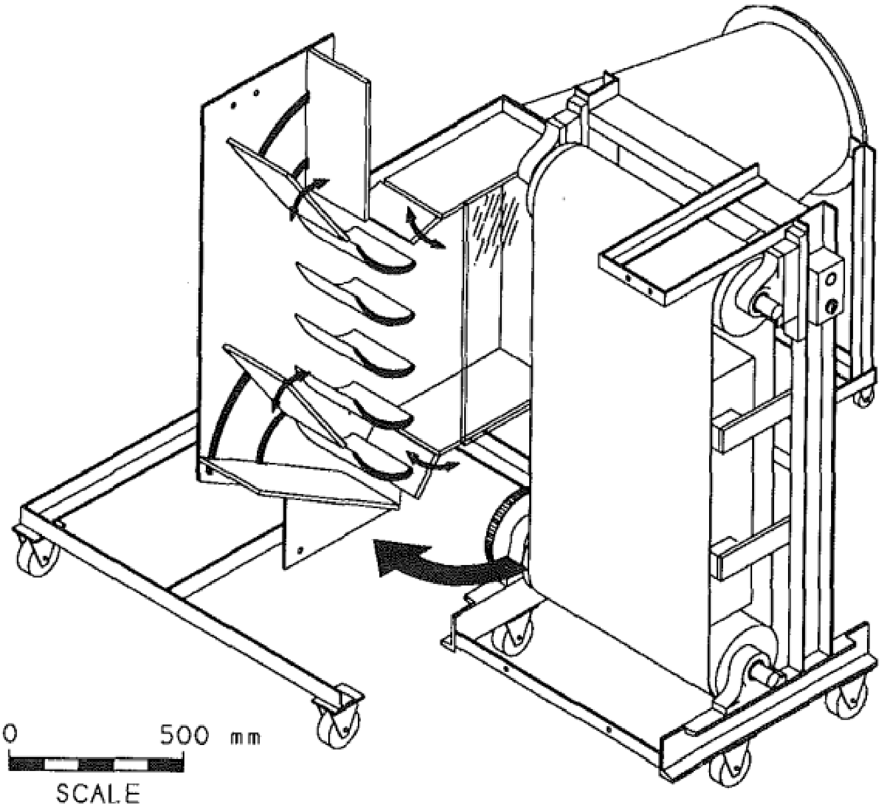

Figure 1.2 Driving belt for simulation of rotation on turbine cascade

2 Principles of fluid dynamics

This part of the work provides a review about the physical principles that rule the fluid flow phenomena. The following parts are going to describe the different fields that are relevant for the theoretical approach of the thesis (Ferziger, 2002).

2.1 Fundamental equations

Fluid flow can be studied from two different points of view, according to the characteristics of the subject; the content can be defined by stationary (Eulerian) or by moving (Lagrangian) coordinate system. In general these two systems present the continuity, momentum, and energy equation. In our study, the Eulerian framework is taken.

2.1.1 Continuity equation

For a fixed fluid element, the mass is conserved according to the physical principle:

$$\frac{\partial \rho}{\partial t} + \nabla \cdot (\rho u) = 0 \tag{2.1}$$

2.1.2 Momentum equation

Based on the Newton's Law, the momentum equation links the fluid particle acceleration to the surface forces and body forces experienced by the fluid:

$$\frac{\partial (\rho u_i)}{\partial t} + \nabla \cdot (\rho \mathrm{u_i} u) = \nabla \cdot \mathbf{T}_s + \rho \mathrm{b} \tag{2.2}$$

where b represents the external forces acting on the fluid element. The stress tensor $\mathbf{T_s}$, which is the molecular rate of transport of momentum, can be written as:

$$\boldsymbol{T_s} = -\left(p + \frac{2}{3}\mu \nabla \cdot \mathrm{u}\right)\mathrm{I} + 2\mu \mathrm{D} \tag{2.3}$$

where μ is the dynamic viscosity, I the unit tensor, p the static pressure and D is the strain rate.

2.1.3 Energy equation

For a fluid element, the energy conservation is expressed by internal energy ρe due to random molecular motion and kinetic energy $(\rho|u|^2)/2$ because of the translational motion of the fluid element as:

$$\frac{\partial}{\partial t}\left[\left(\rho\left(e+\frac{|u|^2}{2}\right)u\right)\right]+\nabla[\rho u\left(e+\frac{|u|^2}{2}\right)u)]=-\nabla\cdot\dot{q}+\rho\dot{q}_s+\nabla\cdot(T\cdot u)+\rho b\cdot u \tag{2.4}$$

Applying the definition of enthalpy $h=e+p/\rho$, the (2.4) becomes:

$$\frac{\partial\rho h}{\partial t}+\nabla\cdot(\rho u h)+\frac{\partial\left(\rho\frac{|u|^2}{2}\right)}{\partial t}+\nabla\cdot\left[\rho u\frac{|u|^2}{2}\right]-\frac{\partial p}{\partial t}=-\nabla\cdot\dot{q}+\rho\dot{q}_s+\nabla\cdot(T\cdot u)+\rho b\cdot u \tag{2.5}$$

where $\dot{q}$ represents the heat flux.

2.2 Turbulence overview

In nature and in engineering, fluid flows present mostly a turbulent behaviour. Irregularity, chaotic nature and instability are the main characteristics of the turbulent flows; at the same time, these properties are notable for the heat, mass and momentum transport values. Chaotic motion and swirling regions, called eddies or vortexes, empower the mixing of the flow, being useful when phenomena require chemical mixing or heat transfers.
Non-dimensional parameter, known as Reynolds number *Re*, is used for describing fluid moving. It is defined in (2.6):

$$Re=\frac{uL}{\nu}=\frac{\rho uL}{\mu} \tag{2.6}$$

where L is the characteristic length scale of the flow and ν is the kinematic viscosity. Practically the Reynolds number can be used to characterize the flow regimes; the laminar regime presents a Reynolds number smaller than the critical one Re_{cr} and is dominated by the viscous forces with a smoot motion, while the turbulent flow – above the Re_{cr} – is subjected by inertial forces, with the presence of instabilities and vortexes. A deep knowledge of the topic is collected in many papers, as the one of Bradshaw where turbulence is studied for many branches (Bradshaw, 1996).

For describing turbulence as quantity, it is essential reminding that fluid velocity field varies significantly in both space and time. The absolute flow velocity (Porreca, et al., 2007) is presented:

$$c(t) = \bar{c} + c'(t) \tag{2.7}$$

where $\bar{c}$ is the mean velocity, while $c'(t)$ is the stochastic unresolved unsteadiness due to turbulence (aperiodic or fluctuation).
Instead the conventional definition of the turbulence intensity level Tu is (Porreca, et al., 2007):

$$Tu = \sqrt{\frac{\overline{u'^2} + \overline{v'^2} + \overline{w'^2}}{3\bar{c}^2}} \tag{2.8}$$

Turbulence has got a particular statistical behavior because a single velocity field is influenced complexly by little variations of boundary conditions. To avoid having random solutions by Navier-Stokes equations, repeatability and macroscopic approach are important elements to consider, as also Pope suggests in his book (Pope, 2000).

2.2.1 Boundary layer

A boundary layer is a thin layer of viscous fluid close to the solid surface of a wall in contact with a moving stream in which (within its thickness δ) the flow velocity varies from zero at the wall (where the flow “sticks” to the wall because of its viscosity) up to U_e at the boundary, which approximately (within 1% error) corresponds to the free stream velocity. Strictly speaking, the value of δ is an arbitrary value because the friction force, depending on the molecular interaction between fluid and the solid body, decreases with the distance from the wall and becomes equal to zero at infinity. For a deeper knowledge about this topic, a complete boundary layer theory text has to be referred (Schlichting & Gersten, 2017).

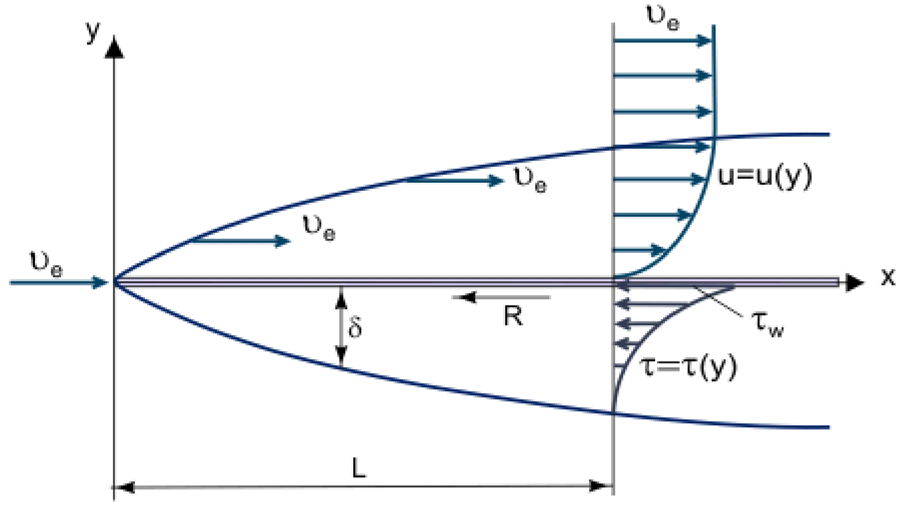

Figure 2.1 Growth of a boundary layer on a flat plate (Epifanov, 2011)

The fundamental concept of the boundary layer was suggested by L. Prandtl (1904). He defines the boundary layer as a layer of fluid developing in flows with very high Re, which is with relatively low viscosity as compared with inertia forces. This is observed when bodies are exposed to high velocity air stream or when bodies are very large and the air stream velocity is moderate. In this case, in a relatively thin boundary layer, friction shear stress (viscous shearing force) is defined as:

$$\tau = \eta \frac{\partial u}{\partial y} \qquad (2.9)$$

where η is the dynamic viscosity, u = u(y) is the "profile" of the boundary layer longitudinal velocity component, may be very large; in particular, at the wall where u = 0 and $\tau_w = \eta \left[\frac{\partial u}{\partial y}\right]_w$ although the viscosity itself may be rather small.

It is possible to ignore friction forces outside the boundary layer (as compared with inertia forces), and on the basis of Prandtl's concept, to consider two flow regions: the boundary layer where friction effects are large and the almost inviscid flow core. On the premise that the boundary layer is a very thin layer (δ << L, where L is the characteristic linear dimension of the body over which the flow occurs or the channel containing the flow, its thickness decreasing with growth of Re), the order of magnitude of the boundary layer thickness can be estimated from the following relationship:

$$\frac{\delta}{L} = \frac{1}{\sqrt{Re}} \qquad (2.10)$$

A laminar boundary layer develops usually at the inlet section of the body. Gradually, under the influence of some destabilizing factors, the boundary layer becomes unstable and transition of boundary layer to a turbulent flow regime takes place. Previous experimental investigations have established the existence of a transition region between the turbulent and laminar regions. In some cases (for example, at high turbulence level of the external flow), the boundary layer becomes turbulent immediately downstream the stagnation point of the flow. Under some conditions, such as a severe pressure drop, an inverse phenomenon takes place in accelerating turbulent flows, namely flow relaminarization. Computation of the boundary layer parameters is based on the solution of equations obtained from the Navier–Stokes equations for viscous fluid motion, which are first considerably simplified taking into account the thinness of the boundary layer.

Many studies have been published, investigating the main points of this topic, like the structure (Townsend, 1950) and the separation of the different layers (Simpson, 1989).

There is a large variety of numerical methods that are used to solve many flow problems to which boundary-layer theory is applied. Two particular methods, the Crank-Nicolson scheme and the Box scheme, seem to dominate in most practical applications (Keller, 1978).

2.2.2 Secondary flow

Secondary flow is produced when a streamwise component of vorticity is developed from the deflection of an initially sheared flow. Such secondary flows occur when a developed pipe flow enters a bend, when a sheared flow passes over an airfoil of finite thickness or over an airfoil of finite lift, or when a boundary layer meets an obstacle normal to the surface over which it is flowing. One of the most important engineering aspects of secondary flow occurs in axial turbomachinery aerodynamics, where boundary layers, growing on the casing and hub walls of the machines, are deflected by rows of blades, stationary and rotating (Horlock & Lakshminarayana, 1973).

Then solutions for the secondary velocity fields are discussed and they have been classified (Hawthorne, 1967). The two parameters of importance are the magnitude of the entry shear and the deflection of the flow. Thus four flows may be considered:

i. small shear, small disturbance in which the Bernoulli surfaces are undistorted and the disturbance is irrotational
ii. small shear, large disturbance in which a primary irrotational flow convects the Bernoulli surfaces and the vortex filaments (this is referred to "secondary flow approximation" and is the one most commonly used to describe secondary flows in turbomachines)

iii. large shear, small disturbance in which the disturbance is rotational and the Bernoulli surfaces are distorted (an example of this approximation is the shear flow through thin airfoils)
iv. large shear, large disturbance, where very few solutions exist.

Secondary flow has been deepened and disparate applications and experimental test rigs have been investigated about this theme, as described in the paragraph 1.2.

From the secondary flow, the main tangible effect of this phenomenon is introduced. Vortexes and eddies represent an important feature of the fluid flows, hardly predictable and influential on aerodynamics and thermal behaviour. All three-dimensional and vortical flow structures developed in turbine passages, due to the presence of 3D effects, angles of attack, non-uniform inlet pressure profiles and unsteadiness together with streamline curvature effects are called secondary flows. Different types of vortexes can be generated and several theories have tried to explain and classify them. Here, a part of work of Ilieva (Ilieva, 2017) is reported: different theoretical approaches are researched during the past scientific papers and are collected to demonstrate the complexity of this topic (Figure 2.2). For a deeper learning about interaction between secondary flow and vortexes, many previous works can be read. Some of them are proposed in the section about the state of the research (Paragraph 1.2).

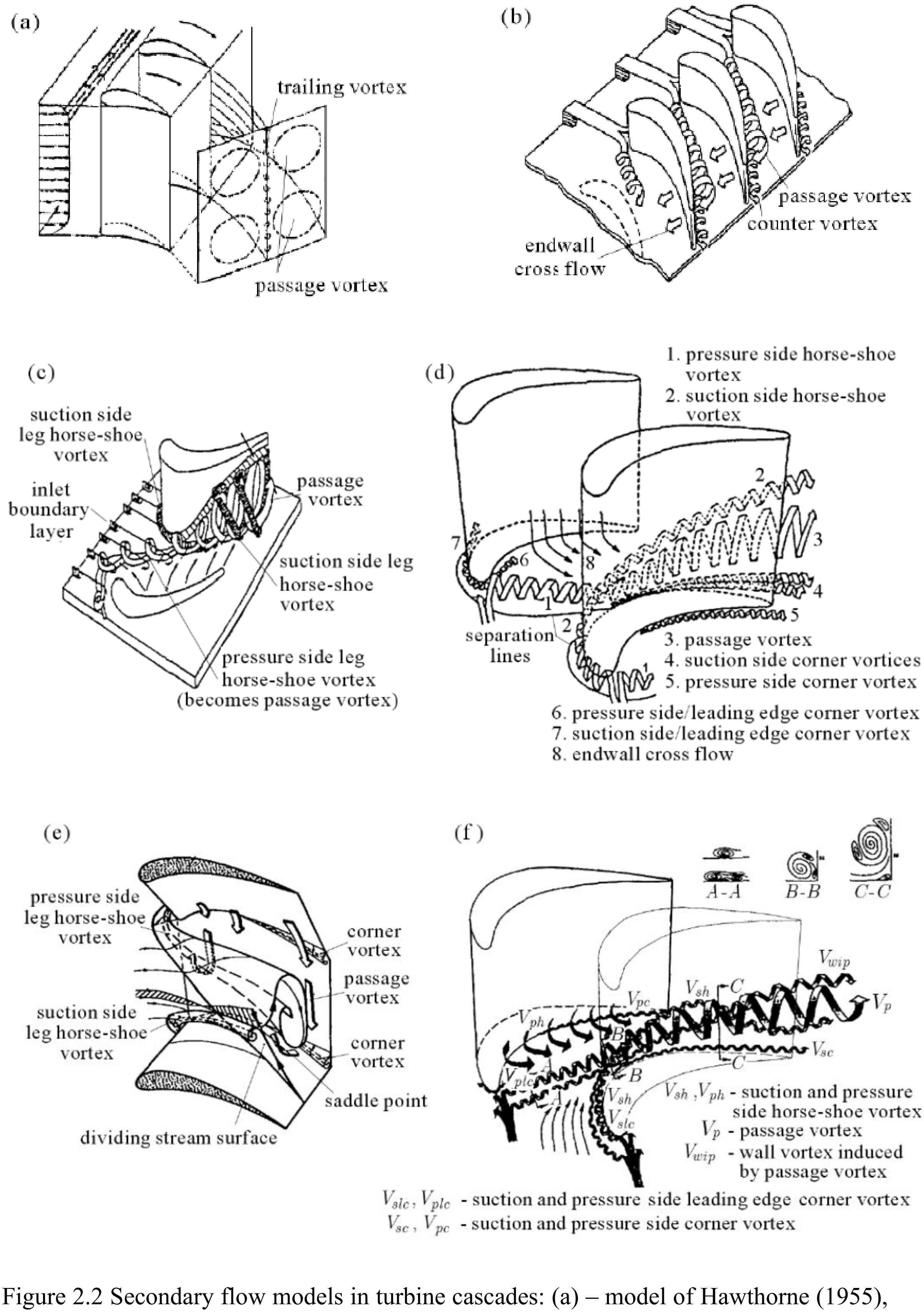

Figure 2.2 Secondary flow models in turbine cascades: (a) – model of Hawthorne (1955), (b) – model of Langston (1980), (c) – model of Sharma and Butler (1987), (d) – model of Goldstein and Spores (1988), (e) – model of Doerffer and Amecke (1994), (f) – model of Wang *et al*. (1997), pictures taken from Lampart (Lampart, 2009)

3 Principles of numerical simulations

Analysis and modelling of turbulence is one of the main goals of the computational fluid simulations. The numerical simulation is applied when a physical problem that describes a fluid flow needs to be solved. The eventual solution cannot be obtained by the analytical resolution of Navier-Stokes equations due to the difficulty of coupled partial equations. Therefore the numerical discretization and simplification models assume great importance to solve flow mechanics issues with a reasonable computational effort.

Direct Numerical Simulation (DNS) solves analytically full Navier-Stokes equations. This method has a relevant impact on a computational mesh fine enough to capture the Kolmogorov scale vortices. To get the mean velocity or any other relevant flow statistics, the time-resolved steps are aggregated accordingly. The number of mesh elements in a mesh required is high and increases with Reynolds number. DNS yields correct physical results; on the other hand, due to the extensively high computational cost of DNS, it is only feasible for simple geometries in low *Re*. Turbulent fluctuations are determined by different models to reduce the time and space resolution.

Large Eddy Simulation (LES) allows the resolution of the governing equations in time using a spatial mesh that captures the large scales of the flow field eddies without being able to resolve the smallest scales. This method is less expensive than the DNS because computes the results on a coarser mesh and with a larger time step, leading to acceptable computational cost for practical engineering systems with complex geometry or flow configurations. Although LES computational cost is still at high levels, it requires resources for high performance computing. Another kind of simulation is Reynolds Averaged Navier-Stokes (RANS), where the time behaviour of the variable is not fundamental while their average has got the most of the interest; at the same way, turbulent fluctuations are not highly considered. For the previous reasons, RANS simulation is cheaper than DNS and LES but it pays in terms of accuracy, especially for complex problems.

3.1 Numerical mesh and stability criterion

One of the main steps of a CFD simulation is the mesh construction. It affects the results as a fundamental parameter of the process. The mesh defines the discrete locations where the variables are to be calculated and it is practically a discrete representation of the geometric domain of the problem.

Mesh can be structured and unstructured, according to the type of grid; Figure 3.1 shows the graphical differences between the two types.

There are several quality criteria for the generation of the mesh. The aspect ratio is the ratio of the shortest to the longest length of computational cells, where values greater than 0.3

should be achieved. Orthogonal distortion compares the line which connects two cell centres and the normal on the common edge of the cells. The optimal value is 0°. Instead, skewness represents the angular measure of element quality concerning the angles of ideal element types; the minimum angle within an element should not be less than 20°.

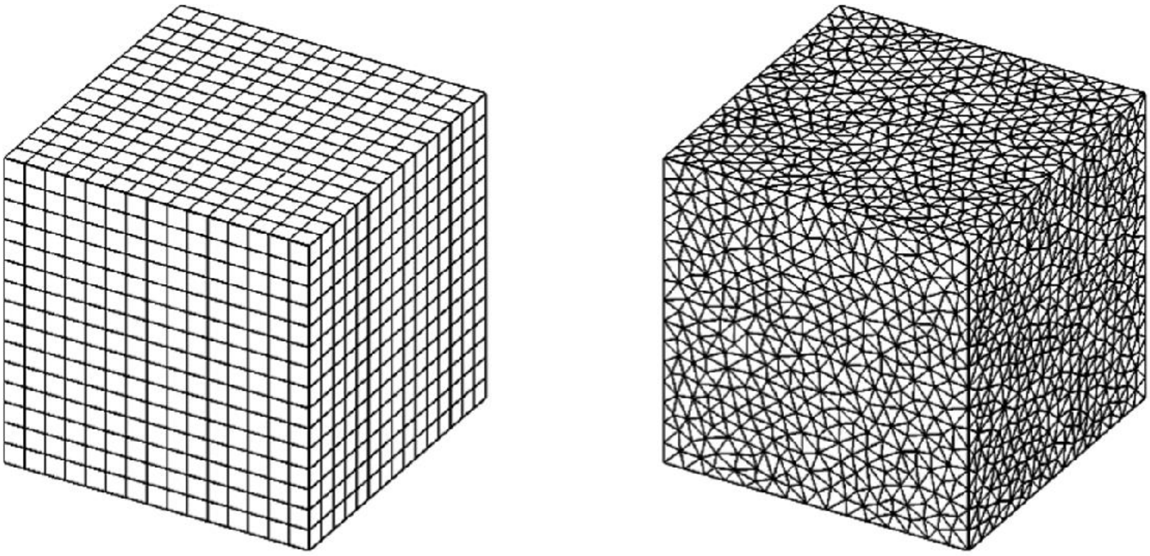

Figure 3.1 a) Example of structured mesh b) Example of unstructured mesh

After the space, time is managed by definition of time steps. For transient simulations, the choice of the time step influences the stability of the simulation, the final flow field and the physical computational time. The criterion of Courant, Friedrich and Levy (CFL number) relates step time to the flow field and the mesh cell length. This criterion is only introduced because simulation of this thesis will be steady-state, so time will be not involved.

3.2 RANS Simulations

RANS simulations follow equations that rule the variables averaged on time; in particular, defining $\alpha(x,t)$ as general variable, they can be considered as the sum of the mean component on the time $\bar{\alpha}(x)$ and the fluctuating one $\alpha'(x,t)$, which still depends on time.

$$\alpha(x,t) = \bar{\alpha}(x) + \alpha'(x,t) \tag{3.1}$$

where:

$$\bar{\alpha}(x) = \frac{1}{\Delta t}\int_{t_i}^{t_i+\Delta t} \alpha(x,t)dt \tag{3.2}$$

The integer at (3.2) is possible if the considered time interval Δt is greater enough than time considered for fluctuations.

With this assumption, the turbulent fluctuations $\alpha'(x,t)$ are statistically independent, which means that their mean value is equal to zero. In a quadratic nonlinear term case, correlation terms with a term that is zero are obtained only when the two quantities are uncorrelated. From this step, the conservation equation is manipulated for achieving two terms: Reynolds stress $\rho\overline{u_i'u_j'}$ and the turbulent scalar flux $\rho\overline{u_i'\alpha'}$. Using the mass-averaging, we can utilize an average velocity factor:

$$\tilde{u}_i = \frac{\overline{\rho u_i}}{\bar{\rho}} \tag{3.3}$$

With this factor, the averaged continuity and momentum equations can be written in a different version:

$$\frac{\partial \bar{\rho}}{\partial t} + \frac{\partial(\bar{\rho}\tilde{u}_i)}{\partial x_i} = 0 \tag{3.4}$$

$$\frac{\partial(\bar{\rho}\tilde{u}_i)}{\partial t} + \frac{\partial(\bar{\rho}\tilde{u}_i\tilde{u}_j)}{\partial x_j} + \frac{\partial(\overline{\rho u_i'u_j'})}{\partial x_j} = -\frac{\partial \bar{p}}{\partial x_i} + \frac{\partial \tilde{\tau}_{ij}}{\partial x_j} + \tilde{B}_i \tag{3.5}$$

Where $\tilde{\tau}_{ij}$ represents the terms of the stress tensor.

Unluckily, the system of equations is not solvable and suitable approximations must be exposed by introducing a turbulence model to approximate Reynold’s stresses. In the mass averaging energy equations, further correlation terms appear. They represent physical processes or variables as the turbulent heat flow, the specific turbulent kinetic energy or the turbulent dissipation rate. In the present thesis, the two-equation turbulence model SST is used. The shear stress transport (SST) formulation combines the advantages of k-ω and k-e models, balancing their respective drawbacks, but this topic will be seen properly in the next paragraph.

3.2.1 Turbulence numerical models

Development of CFD software has tried to deal with complex problems as turbulence. Improvement of computational strength allows now to manage different kinds of turbulence situations, according to the specific case and applying the right and coherent approximations. About this subject, in this paragraph a little introduction of turbulence numerical models is made; details are reported from the ANSYS CFX manual, which can be explored for further details (ANSYS, Inc., 2009).

The simplest model manages very simple eddy viscosity models, which compute a global value for μ_t from the mean velocity and a geometric length scale using an empirical formula. Because no additional transport equations are solved, these models are indeed termed "zero equation". The zero equation model in ANSYS CFX uses an algebraic equation to calculate the viscous contribution from turbulent eddies. A constant turbulent eddy viscosity is calculated for the entire flow domain.

An upgrade is possible when two-equation turbulence models are implemented. They offer a good compromise between numerical effort and computational accuracy. Two-equation models are much more sophisticated than zero equation models. Both the velocity and the length scale are solved using separate transport equations, which give the name. The k-ε and k-ω models exploit the gradient diffusion hypothesis to link the mean velocity gradients and the turbulent viscosity to the Reynolds stresses. The product of turbulent velocity and turbulent length scale is the modelling of the turbulent viscosity. The transport equation provides as solution the turbulent kinetic energy that is necessary to compute the turbulence velocity scale; the turbulent kinetic energy and dissipation assume the role of properties for evaluating the turbulent length scale.

Some particular two-equation models – relevant for this thesis – are listed:

- the k-ε model, where k is the turbulence kinetic energy and is defined as the variance of the fluctuations in velocity; ε is the turbulence eddy dissipation
- the RNG k-ε model, which is modelled on renormalization group analysis of the Navier-Stokes equations. The transport equations for turbulence generation and dissipation are the same as those for the standard k-ε model, but some model constants differ
- the k-ω model, which has the advantage of the near treatment for low-Reynolds number computations. It is based on the correlation between turbulence kinetic energy and turbulent frequency as $\mu_t = \rho \frac{k}{\omega}$. The most common k-ω models are Wilcox k-ω model, the BSL k-ω model and SST model. The last one explains the transport of the turbulent shear stress and provides accurate predictions of the onset and the flow separation for adverse pressure gradients.

On the other hand, Reynolds Stress turbulence models can be adopted; they are based on transport equations for all components of the Reynolds stress tensor and the dissipation rate. They solve an equation for the transport of Reynolds stresses in the fluid and are not based on eddy viscosity hypothesis. They can be considered more suitable to the complex fluid flows because they produce exact terms and the relative modelling of stress anisotropy.

4 Numerical model

After a presentation of the general knowledge useful for understanding the fundamentals of this thesis, the particular case is presented. The work concerns the study of the influence of the rotation on different parameters that represent the aerodynamic behaviour of the air flow. The process is practically made via Computational Fluid Dynamics (CFD) software and has the goal of showing the relevance of rotational speed on the current experiment, for justifying the eventual negligibility of it. As collateral consequence, providing more knowledge and important hints for future similar works and upgrading investigations could be an added value, especially about the thermal and heat transfer process. The numerical investigation allows to simulate a configuration that would be very expensive for a basic prototype or a study case; in any case, it is not currently reproducible for the planar configuration. Technology of CFD is determined in this case and it is developed along several phases:

i. design of a geometry that reproduces the content of the investigation and its domain
ii. processing a mesh to optimize the task without losing precision and accuracy of results, with an optional consequent mesh convergence analysis
iii. application of the initial and boundary conditions and application of a complete setup for simulating the correct situation
iv. analysis of the outcomes thanks to post-processing tool and presentation of results
v. comparison of different settings.

4.1 Geometry

First step of the study is about the design of the model, which represents the experiment apparatus, by Computer Aided Design (CAD) software. In this case, the file was a preceding project by Marco Hahn, the owner of the experiment and co-supervisor of this thesis. Siemens NX was used for this phase.

The Figure 4.1 shows the experimental designed test rig, as a planar base with a cascade of 4 airfoils, in its first step, arranged to permit the air to be deviated. The project will be modified in the future adding some cavities on the base for construction reasons. These elements could be interesting for studying the cooling of the high temperature fluid flow. The shape of the apparatus presents an important stagger angle; on the other hand, air flow of the simulation – as velocity direction at the inlet – is set to have incidence close to zero in the static case. For the study, only one central airfoil will be studied, with empty channel upstream and downstream, respectively long ${L_{up}}/{C} \approx 0.9$ and ${L_{down}}/{C} \approx 0.55$, if measured in parallel to the X axis (Figure 4.3).

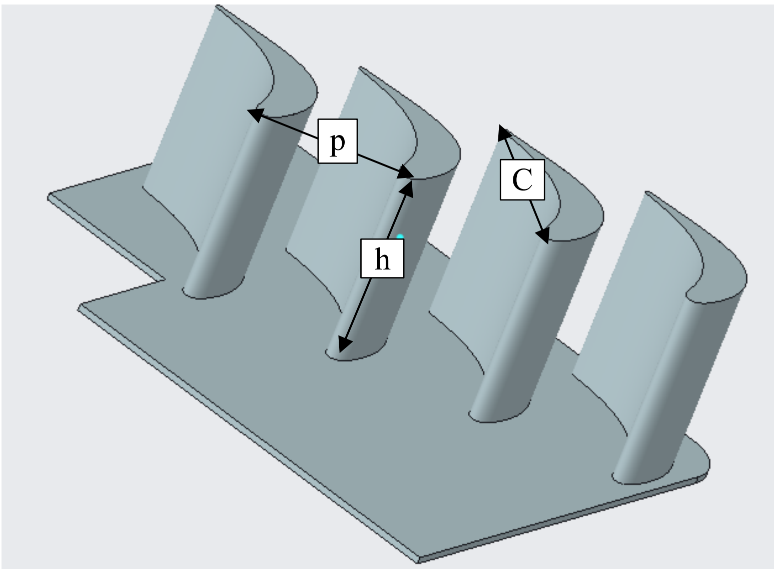

Figure 4.1 Geometry of turbine cascade

Pitch p=78.0 [mm] Height h=128.1 [mm] Chord C=117.3 [mm]

4.2 Mesh

After the comprehension of the geometry, numerical part takes place in this chapter. Mesh Generation Software Pointwise is used for this part. For the numerical study, the structured mesh is chosen, so it is seen as a regular grid with 4-sided polygons on 2D and hexahedrons on 3D (Figure 3.1). The mesh is characterized by a refinement close to the upper wall, lower wall, sides and airfoil, to study better the velocity field in the zones where there are conditions of no slip wall and periodicity (Figure 4.2). The spacing was computed taking into account the tool by Pointwise, which outcomes a value of Δs from different parameters, as length and mostly y^+. The wall y^+ is a non-dimensional number similar to local Reynolds number, determining whether the influences in the wall-adjacent cells are laminar or turbulent, hence indicating the part of the turbulent boundary layer that they resolve (Ariff, et al., 2009). It is defined as:

$$y^+ = \frac{u_{\tau,air} y}{v_{air}} \tag{4.1}$$

where $u_{\tau,air}$ is friction velocity, y is the orthogonal coordinate and v_{air} is the velocity of the flow. In this case, the y^+ is kept below 1.

For obtaining the best compromise between the computational expense and the precision of the results, 5 different meshes are proposed with increased number of cells: obviously the greater the number of hexahedrons, the finer the spacing of the refinement (Table 4.2). Decision about the right mesh will be postponed after a mesh convergence study, which will give hints for a good a trade-off, in the paragraph 4.5.

Some geometrical features are reported in Table 4.2 to have a deeper overview of the chances. The scientific paper by Aqilah et al. provides a good explanation about the features that are useful for characterizing a mesh and its quality (Aqilah, et al., 2018).

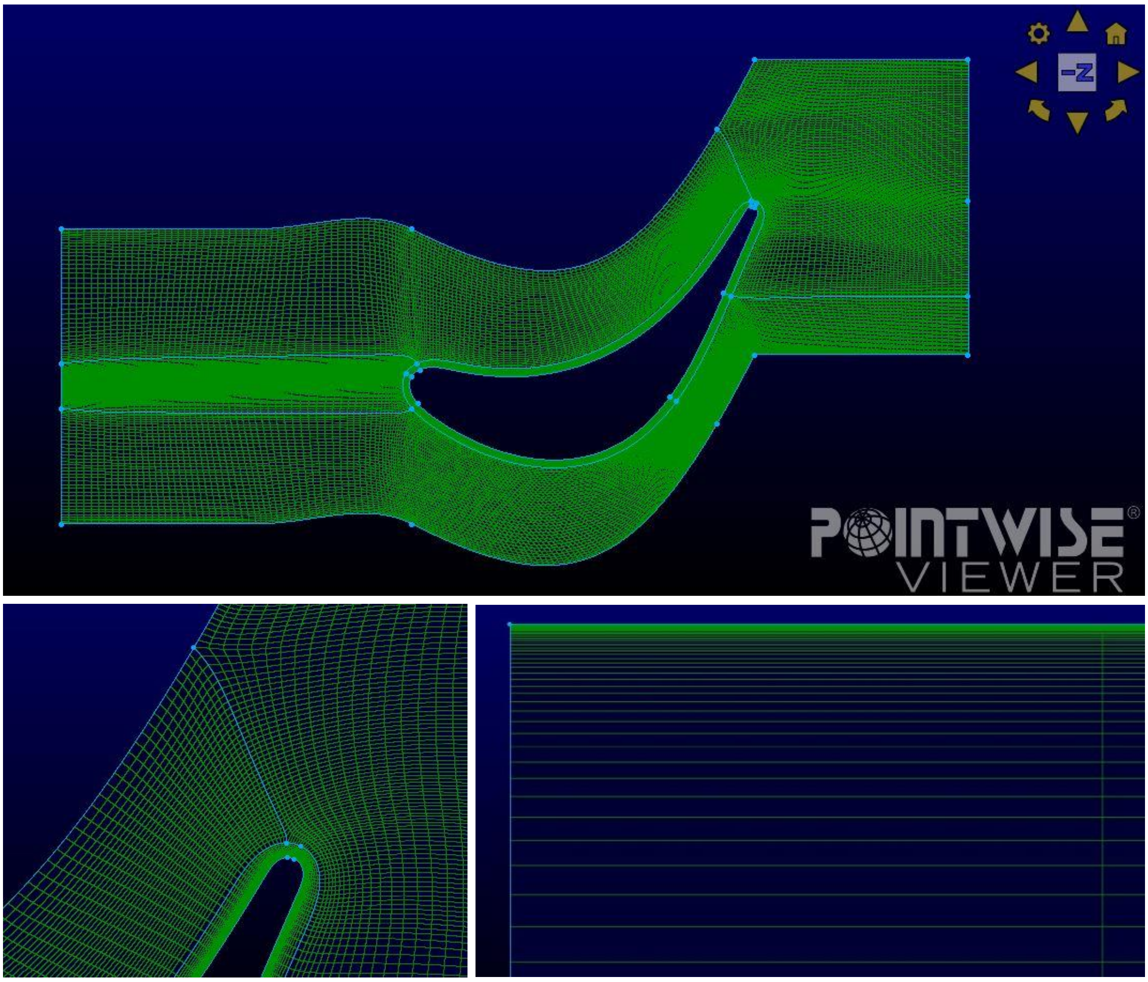

Figure 4.2 a) Mesh overview b) & c) Details of refinement close to airfoil and upper wall

	Nodes	Hexahedrons	Maximum y^+
Coarser	707965	677880	1.8779
Coarse	2579072	2507107	1.0715
Normal	4099952	4002300	0.8833
Fine	5822330	5698849	0.7644
Finer	7178808	7036556	0.6966

Table 4.1 Geometrical charateristics of 5 meshes

	Max aspect ratio	Max Cell non-orthogonality	Max equiangle skewness	Max centroid skewness
Coarser	50.55	67.1153	0.7613	0.6223
Coarse	36.37	66.0055	0.7481	0.6801
Normal	35.83	66.2531	0.7499	0.6116
Fine	30.72	54.7941	0.6831	0.4843
Finer	35.84	89.3401	0.9999	1

Table 4.2 Geometrical features for mesh convergence study

4.3 Boundary conditions

As written before, only one airfoil is studied and the shape of the model is processed by ANSYS CFX. In the section CFX-Pre, boundary conditions are added to the mesh. First, steady-state condition is chosen, the studied fluid is set as ideal gas air, any buoyancy is not applied and RANS is implemented. About the turbulence model, Shear Stress Model is chosen with a turbulence intensity of 5%.

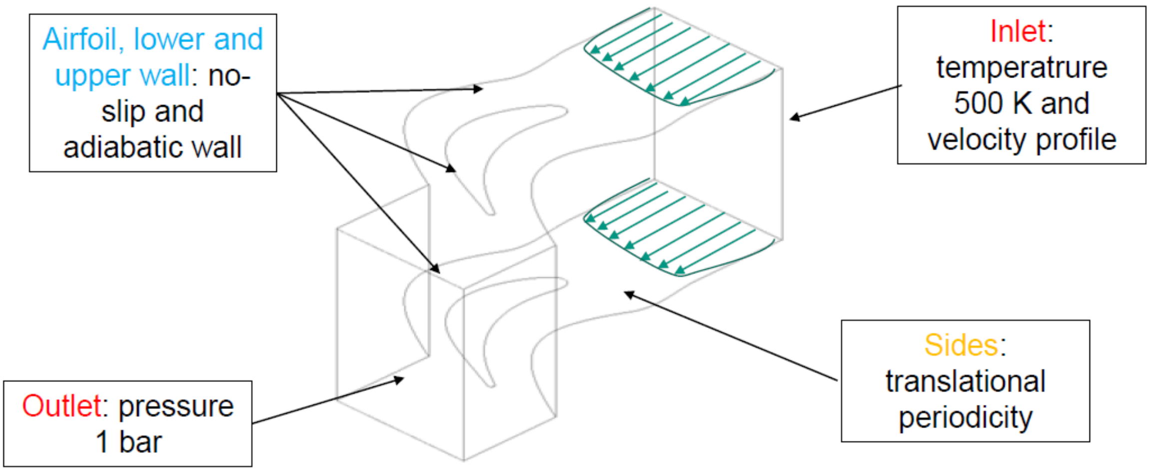

Figure 4.3 Boundary conditions

About the geometry, the inlet temperature is marked out by T=500 K and a velocity profile (Figure 4.4) given by previous studies: the direction of the velocity is overall applied to have almost null incidence – in the first static case – while, along the radial direction, it is presented as a large parabola to fulfill the no slip condition of the upper and lower walls. These last 2 elements present also adiabatic option. On the other hand, the outlet has constrains about pressure, which is set as ambient pressure at 101325 [Pa] (pressure reference: 0 [atm]). Airfoil is simply set as an adiabatic and no slip wall. Differently, lateral sides need more effort: they present a translational periodicity to simulate the serial reproduction of the airfoils to build the cascade, as Figure 4.1.

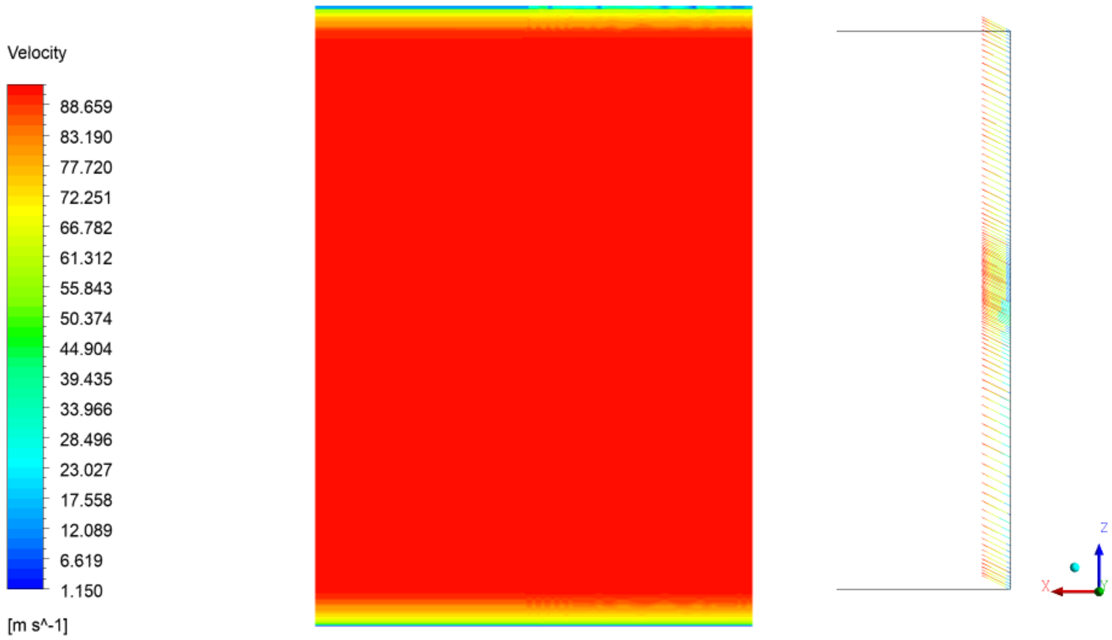

Figure 4.4 Inlet velocity profile

4.4 Subdomain approach

The breakthrough of pre-setting is about the application of rotation. Being a linear model coming from the construction of a cascade, applying just a rotation could be counter-intuitive but mostly inconsistent. In previous years, this kind of approach was studied by Yaras and Solander, which proposed an experimental rig where a planar cascade revolves around, as a conveyor belt (Yaras & Sjolander, 1992), described in the paragraph 1.2; in that case, the reproduction was built to study the tip leakage. Taking inspiration from that scientific paper, in this thesis, numerical application of revolution is simulated by a translational subdomain: rotation is implemented taking care of the linear shape of the model and focusing only on the forces acting on it.
Beyond the flow generated by inlet velocity, rotation is characterized by Centrifugal and Coriolis force. As Brock University (Physics, 2020) describes, they are formulated here:

$$\vec{F}_{fict} = \vec{F}_{centrifugal} + \vec{F}_{coriolis} = -m\vec{\omega} \times (\vec{\omega} \times \vec{r}) - 2m\vec{\omega} \times \vec{v} \qquad (4.2)$$

In an annular case, the forces are analysed following the cylindrical coordinate system:

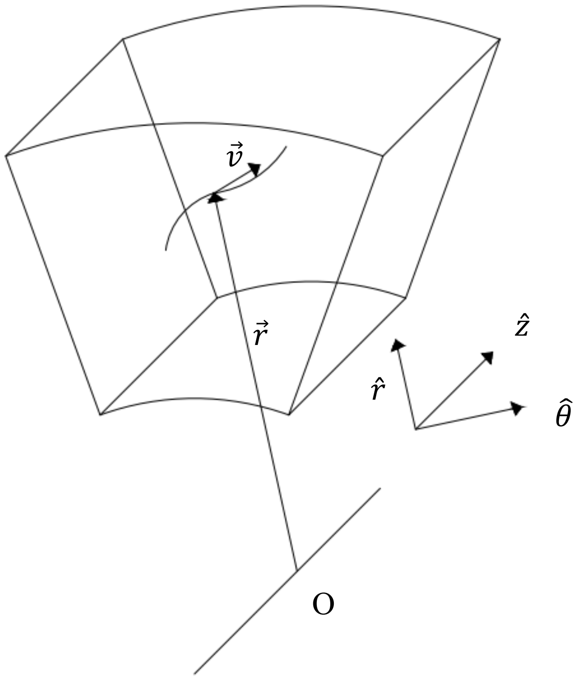

Given the components of the versors:

$$\vec{r} = (r, 0,0)$$
$$\vec{\omega} = (0,0, \omega)$$
$$\vec{v} = (v_r, v_\theta, v_z) \tag{4.3}$$

Centrifugal force is computed as in (4.4), solving the vectorial products:

$$\begin{gathered}\vec{F}_{centr} = -m\vec{\omega} \times (\vec{\omega} \times \vec{r}) = \\ -m\vec{\omega} \times \left(\omega r \hat{\theta}\right) = \\ -m\omega r^2(-\hat{r}) = m\omega r^2 \hat{r}\end{gathered} \tag{4.4}$$

After computations, centrifugal force is obtained, showing that has no null value only along radial direction; instead Coriolis force influences both radial and polar direction:

$$\begin{gathered}\vec{F}_{cor} = -2m\vec{\omega} \times \vec{v} = -2m\omega(-v_\vartheta \hat{r} + v_r \hat{\theta}) = \\ +2m\omega v_\vartheta \hat{r} - 2m\omega v_r \hat{\theta}\end{gathered} \tag{4.5}$$

The result describes the fictitious forces, as combination, in an annular case:

$$\vec{F}_{fict} = \begin{Bmatrix} (2m\omega v_\vartheta + m\omega r^2)\hat{r} \\ -2m\omega v_r \hat{\theta} \end{Bmatrix} \tag{4.6}$$

The same procedure is applied now to the planar case. For it, the forces are analysed following the Cartesian coordinate system. A translation from cylindrical coordinate system to Cartesian coordinate system is applied:

$$\hat{r} \rightarrow \hat{z}$$
$$\hat{\theta} \rightarrow -\hat{y}$$
$$\hat{z} \rightarrow \hat{x} \tag{4.7}$$

The scheme of the new applied forces is:

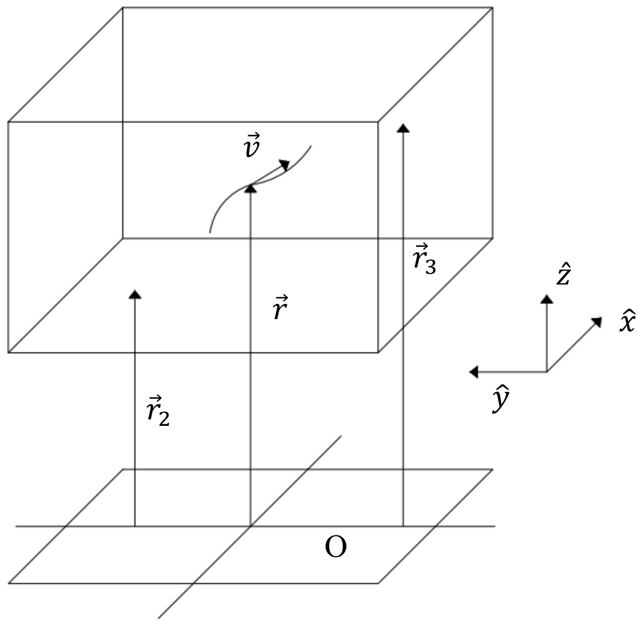

Coordinates are presented as in the numerical model.
Here, the previous passages are replied for the planar configuration. Computation process is the same but the new system gives different results, as shown in (4.11):

$$\vec{r} = (0, 0, r)$$
$$\vec{\omega} = (\omega, 0, 0)$$
$$\vec{v} = (v_x, v_y, v_z) \tag{4.8}$$

$$\begin{gathered} \vec{F}_{centr} = -m\vec{\omega} \times (\vec{\omega} \times \vec{r}) = \\ -m\vec{\omega} \times (-\omega r \hat{y}) = \\ -m\omega r^2(-\hat{z}) = m\omega r^2 \hat{z} \end{gathered} \tag{4.9}$$

$$\begin{gathered} \vec{F}_{cor} = -2m\vec{\omega} \times \vec{v} = -2m\omega(-v_z\hat{y} + v_y\hat{z}) = \\ +2m\omega v_z\hat{y} - 2m\omega v_y\hat{z} \end{gathered} \tag{4.10}$$

$$\vec{F}_{fict} = \begin{Bmatrix} (m\omega r^2 - 2m\omega v_y)\hat{z} \\ 2m\omega v_z\hat{y} \end{Bmatrix} \tag{4.11}$$

This approximation has got a consistent matching, because definition of radius is conserved and also the angle versor is well described by *(-$\hat{y}$)*; the translation of coordinate system is presented for describing the calculi that lead to the planar case formulas. In annular configuration the origin is a point on the axis line of the cylinder, while in a planar system, these features are seen in a different way: origin becomes an horizontal line while the axis is represented by the plane (the figuration of r_2 and r_3 is made for explaining graphically this concept). Trivialising, the planar model can be seen as a laid version of the annular one.

Numerically, the results are reported in a sub-domain of CFX-Pre, created to contain momentum sources that refer to the fictitious forces. In this way, varying the ω, different rotational speed cases are obtained: angular velocity of single points is seen as linear transversal velocity while centrifugal force keeps its property to “run away” from the centre axis.

4.5 Mesh convergence study

After implementation of various initial conditions, the most suitable mesh has to be checked. To get a trade-off between time cost and result’s precision, some quantities are studied in different monitor points, describing middle-span upstream and downstream, before in stationary condition and then in a rotational case with ω=200 rad/s (Figure 4.5). The results give satisfying directions about the choice of mesh. The arrangement 4 (table 4.3) is judged as the best one and, for this reason, it is adopted to study all the following properties of the work.

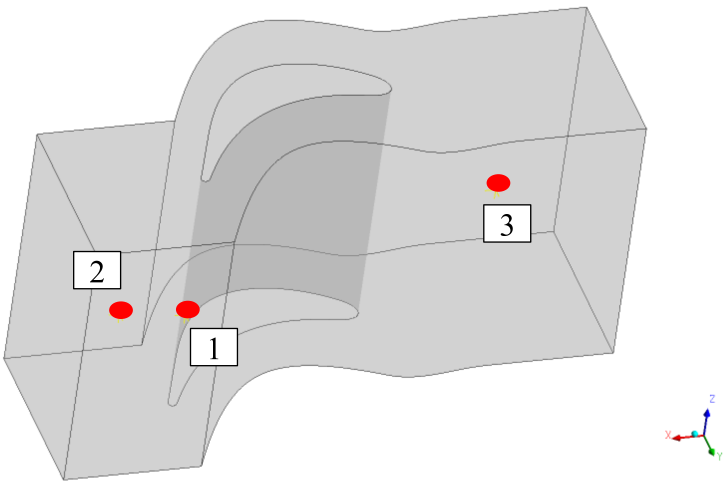

Figure 4.5 Points examined for mesh convergence study

The point 1 follows the wake of the flow and for this reason it could be affected by turbulence activity; points 2 and 3 are respectively the middle pitch point of downstream and upstream zone. In these 3 points, absolute pressure and Mach number are compared. Mass flow rate is instead investigated on 3 planes: inlet plane, upstream plane (plane orthogonal to axial direction that crosses the point 3) and downstream plane (plane orthogonal to axial direction that crosses the point 2). All the values are reached after 100 iterations – necessary to gain a convergence value – with an obvious increase of processing time with the increase of number of cells.

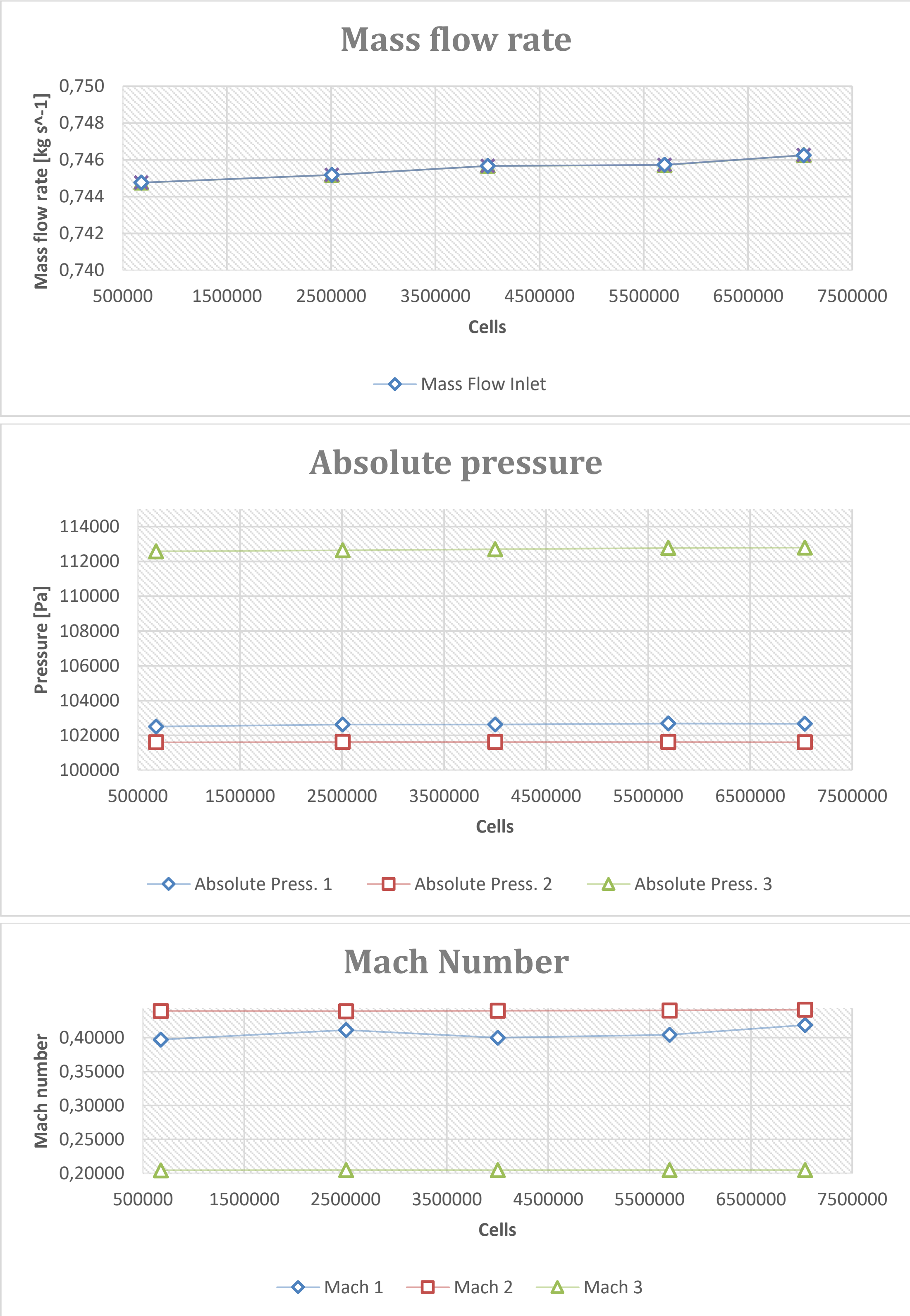

Figure 4.6 Results of mesh convergence study

As you can see from the last graphs of Figure 4.6, noticing of convergence is difficult because values' deviation is almost negligible. Some more detailed examples – which represent well the data sample – are showed in figure 4.7 and Figure 4.8 to justify the choice and the convergence.

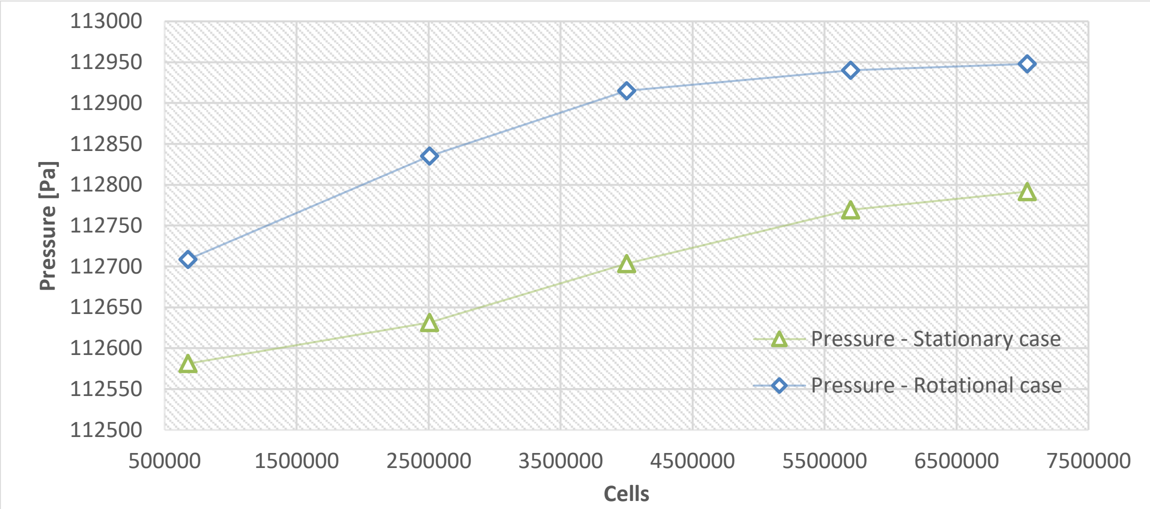

Figure 4.7 Detail of pressure at point 3 for stationary and rotational case

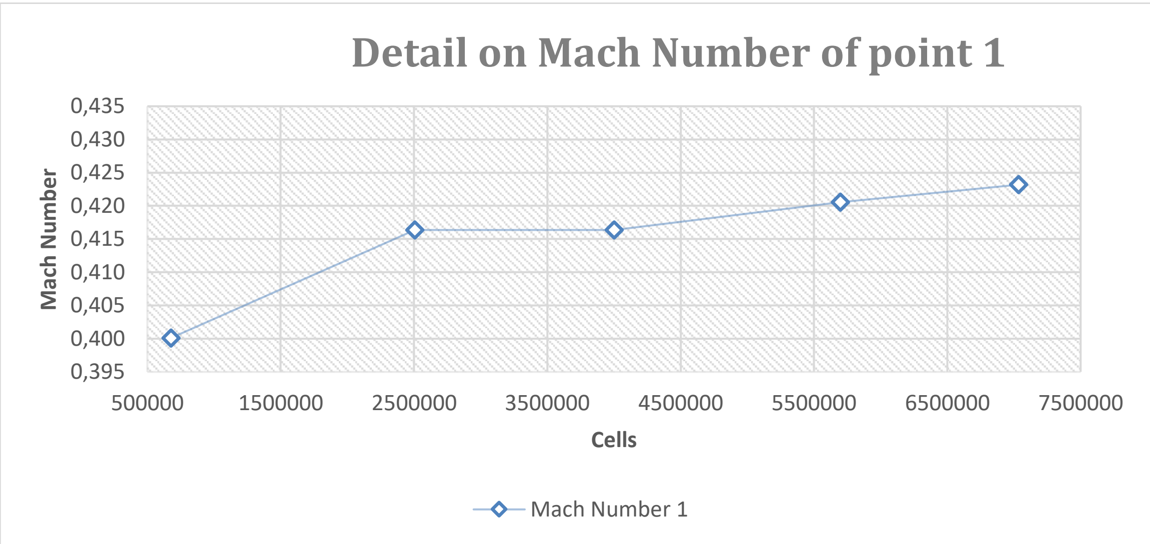

Figure 4.8 Detail of Mach number at point 1 for rotational case (ω=200 rad/s)

As anticipated at the beginning of the paragraph, an important aspect is the comparison of the direct time. In table 4.3, CPU hours for 200 iterations of every mesh are reported. Fine mesh with almost 6 million of cells presents again a good trade-off between the precision of results previously illustrated and the time cost.

	Hexahedrons (cells)	CPU hours
Coarser	677880	0.42
Coarse	2507107	0.99
Normal	4002300	1.87
Fine	5698849	2.35
Finer	7036556	3.96

Table 4.3 Time cost of 5 meshes

4.6 Analysis of different turbulence settings

After the mesh convergence analysis, the right mesh has been selected. In this section, a discussion about the turbulence model to adopt could be enriching. In paragraph 3.2.1., an overview about numerical turbulence models is presented; now in this section, the analysis will be about their cost and their application in the numerical simulation.

Primarily, a non-dimensional factor C_l is employed to compare the different settings. Lift coefficient - often evaluated in the aerodynamics field – is already researched in the scientific paper of Institute of Aerodynamics and Gas Dynamics, which used the same factor for revealing two distinct approaches (Bangga, et al., 2017). The factor was computed as:

$$C_l = \frac{2F_\perp}{\rho A U_\infty^2} \tag{4.12}$$

In this thesis, the lift coefficient is reckoned along 3 different models. The first two files are ruled by the Shear Stress Turbulence model with the difference of turbulence intensity: medium (5%) versus high (10%) one. The third file, instead, is controlled by the Speziale, Sarkar and Gatski (SSG) Reynolds Stress model. A practical application of this kind of model was made to simulate the fluid dynamics in a full baffled stirred tank with a Rushton turbine impeller (Qi, et al., 2010).

In this case, the interest does not concern the turbulence models, but the purpose is the emphasis of a symbolic factor that is really similar for different settings. The all C_l values are studied normalizing to the maximum one (highest rotational velocity case with the application of the SST model characterized by high turbulence).

In the Figure 4.10, it is possible appreciating that values generated by SST model correspond almost perfectly, while the SSG Reynolds Stress differs from them, but never more than 0.8 %. We could affirm that dissimilarity among the results is nearly negligible.

On the other hand, the SSG Reynolds Stress model had got an heavier impact on the time cost, requiring a little less than the double in terms of processing time, keeping the number of iterations constant; the positive response of this model can be gained for analysis about thermal and heat transfer conditions, which are not the main goals of this thesis.

Instead about the compromise of turbulence intensity, the medium arrangement is preferable for this work's approach.

In conclusion, this section provides not only a clarification about the type of chosen turbulence model but mostly some hints for the future works.

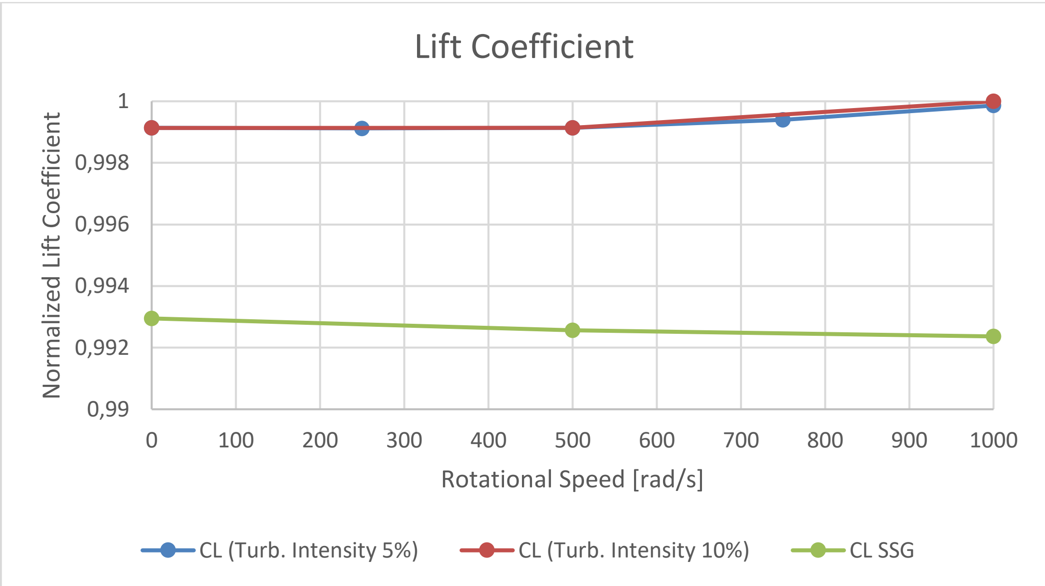

Figure 4.9 Lift coefficient computed for turbulence model analysis

5 Results

In this section, the various results obtained by simulations are summarized. In particular, the following charts, plots and contours will show different behaviours of the flow and how factors, mostly linked to secondary flow and vorticity, change according to the independent variables, especially rotational speed. All the conclusions are reaped mostly from the post processing phase and are compared to scientific papers, to highlight differences and similarities with close cases and experiments.

The rotation is going to be applied with 4 different values: 250 rad/s, 500 rad/s, 750 rad/s, 1000 rad/s. The different rotational velocity cases will be recalled by the percentage with respect to the maximum velocity. Practically this operation is implemented varying the value of ω, as explained in the paragraph 4.4. The stationary case (ω=0 rad/s) will be presented as well, to highlight the effects of rotation. The rotating radius is set fixed at 0.65 [m] for every case, to keep an aspect ratio of $\frac{h}{d} \approx \frac{1}{10} = 0.1$.

Different lines and planes will be used, according to the need, because studied variables can be highlighted in different ways, for the locations and for the goal of the discussion.

In the second part of this paragraph, some non-dimensional coefficients presented in paragraph 1.2 will be studied and some results will be showed.

This crossover discussion has got the aim to provide a full overview of the study and a moderate knowledge about the influence of the rotation and the relative forces on the aerodynamics of the flow, in order to neglect or not this variable from the study taken by ITS.

5.1 Pressure at airfoil

This first part provides data about the values of pressure around the airfoil. The blade is analysed at middle height $\frac{z}{h} = 50\%$ (green line of Figure 5.2), and the graph plots the values of pressure along the axial direction, for different rotational speeds.
The trend of the values is very similar also if there is a global increase of pressure for every point with increasing of rotational speed. A previous scientific work about multistage radial inflow turbine (Li & Zheng, 2006) shows some similarities with the obtained data: the shape of the blade surface pressure is close to the simulation of this study and moreover in both plots there is an adverse pressure region in the final part. This last property has to

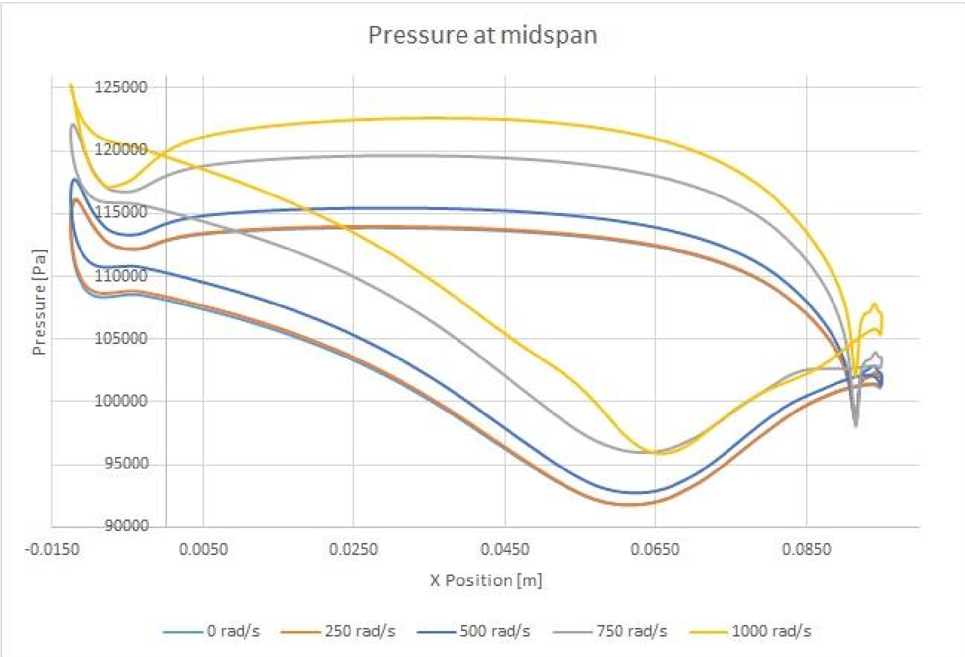

Figure 5.1 Pressure of airofil at midspan for studies rotational speed cases

warn the design because exhibits a crucial zone for the flow, close to the final part of suction side.
The main difference is the load type because the profile studied by Li and Zheng has a front load one. The present study shows that profile manages a great difference of pressure in the rear part, due to its conformation.
The minimum pressure peak moves for different velocity cases; it gets closer to the trailing edge with the enhancement of the rotational speed. Along the central part of pressure side the value remains almost constant. The trend becomes more unstable close the leading edge (the maximum pressure peaks are present) and the pressure fluctuates due to the critical point of the incidence. Indeed, in the highest rotational case, an adverse pressure zone close to the leading edge is present.

5.2 Outflow angle

Another important aspect of the flow that crosses a turbine stage is the outlet behaviour. This zone is dominantly characterised by vortex shedding and high turbulence load. A particular parameter, the outflow angle, is studied to have an overview about this kind of unpredictability.

The value is found searching for the direction of the velocity in the plane orthogonal to the radial direction. It is expressed keeping axial direction as reference and adopting the deviation of the outflow as positive angle. This value is presented in three different lines parallel to the radial direction, arranged in the positions showed in Figure 5.2.

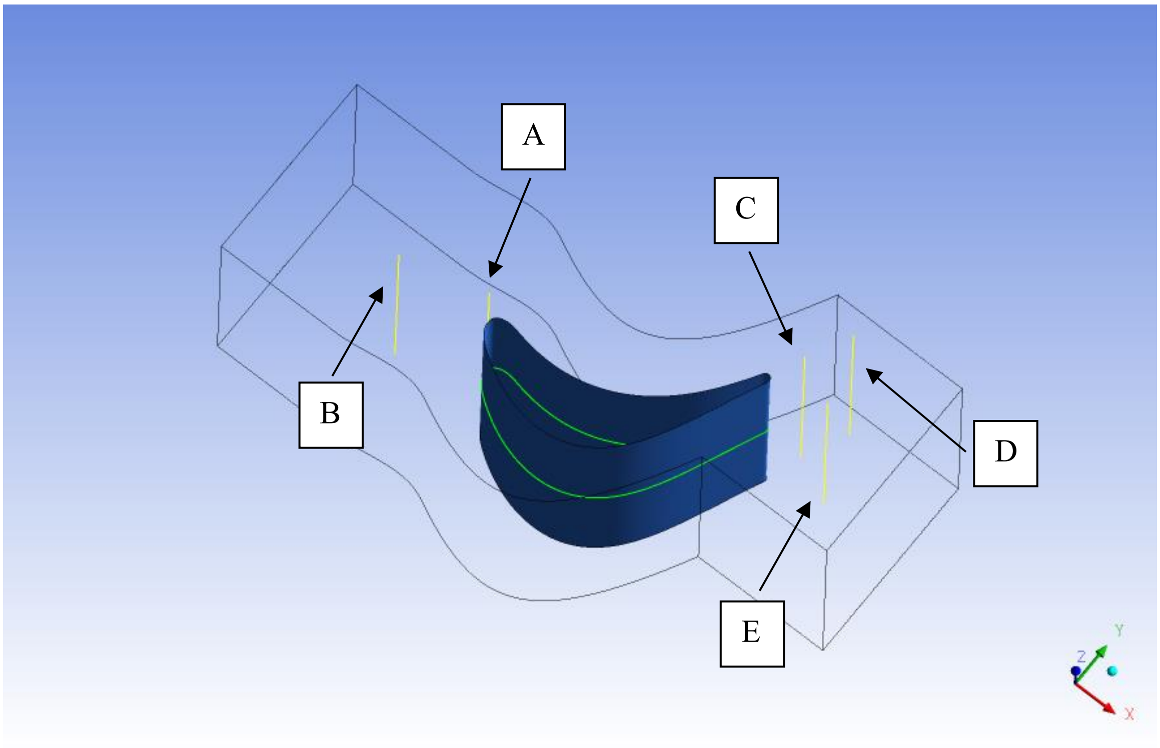

Figure 5.2 Explanation of the lines used for the computation

A. Inflow 1
B. Inflow 2
C. Outflow 1
D. Outflow 2
E. Outflow 3

The choice of the lines position is given by the willing of investigating the direction of the flow in different points of downstream channel. In particular the first two plots highlight the direction of the velocity in 2 lines along the wake (Figure 5.3 (a) and (b)), to emphasize the presence of the eddies and the effect of turbulence; on the other hand, the third plot represents the behaviour of the flow in a region not close to high vorticity (Figure 5.3 (c)).

For simplifying the comprehension, there is a plot with the reference stationary profile (set at 0 rad/s), for every position (Figure 5.3 (d)). This reference plot provides the outflow angle for different outflow positions, showing the no application of rotation: the trend is symmetric due to no slip conditions of upper and lower walls. In addition, the consistency of the values is broken only by vortex shedding that is visible close to the walls.
A similarity in the shape of the trends is considerable due to the constant values at middle height while a swinging profile in the upper and lower zone is noticed. Nevertheless, the outflow in position number 3 does not follow this behaviour in a proper way, as the other ones. The change of positive and negative increment of the angle that is seen in the extremities stands for vortexes effect.
Analysing now the influence of the rotational speed, the plots at Figure 5.3 (a) and (b) are described. Both results present a vertical line that is the main direction of the flow; for the stationary model, changes of direction – physically vortexes – occur in the upper and lower $\frac{z}{h} = 23{,}2\%$ and $\frac{z}{h} = 28{,}6\%$, symmetrically. This approach varies radically when rotational speed is increased: the lower vortexes move upwards, giving more space to ones close to the hub, while the upper vortexes are compressed to the tip wall. For the outflow line 1, the variation of angle direction is positive for the bottom part while is negative for the top one, with respect to the modal value. The increment of deviation gets almost 30 degrees for the fastest case, with two evident peaks (in the slowest cases, only 75% velocity case profile has got them, but they are different), while the reduction of angle deviation follows a trend, which connects all the negative bumps. For the second plot, a consistent accentuation of instability is visible in the upper half for high velocities cases with a strong decrease of the angle of the flow; decrease is even stronger than previous case because the modal outflow angle value is shifted by about 5 degrees.
Different matter for the third plot (Figure 5.3 (c)), where the analysis is made in an area far from the trailing edge, from wake and from vortexes: in this position, the change of angle is almost linearly proportional in the 100% velocity case setting, while, in the lower velocity ones, the inclination is weaker keeping more vertical shape due to the strength of modal value. The great deviation is detectable in zone close to the hub. For low velocity cases, the changes of direction are not so sudden and the variation is smooth.

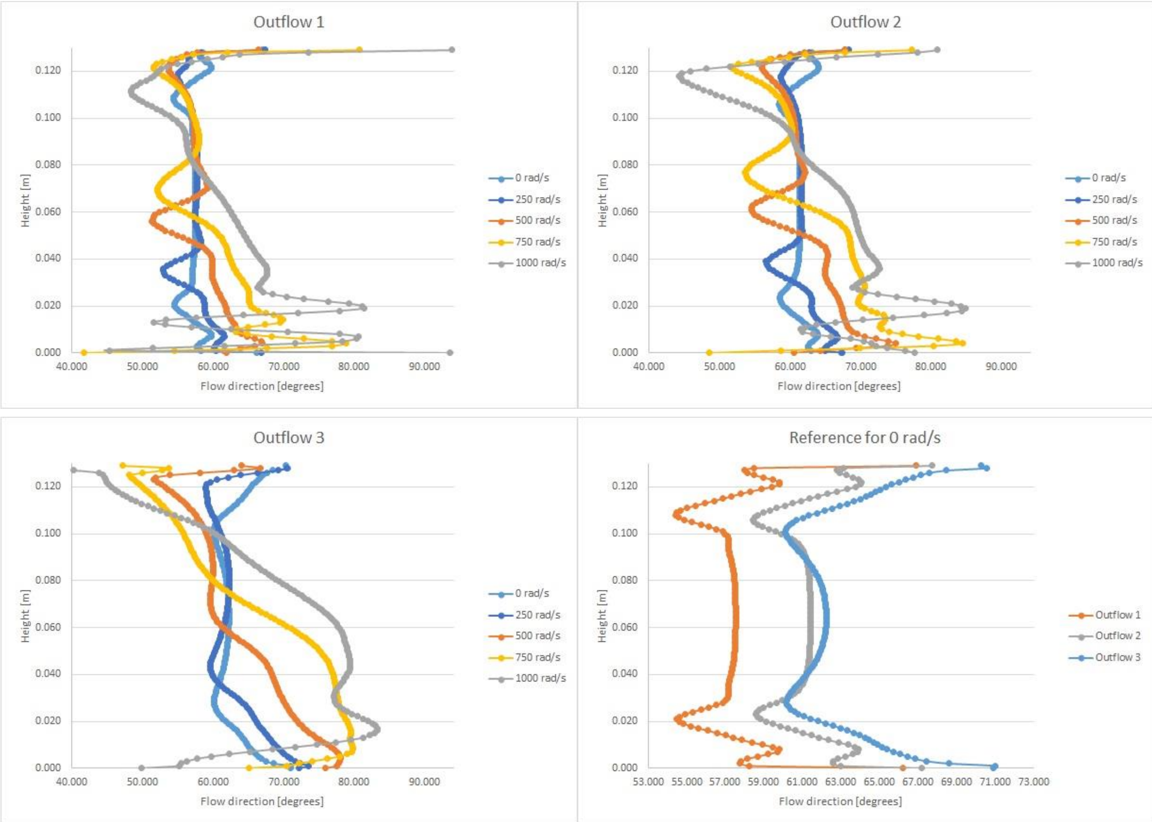

Figure 5.3 a) Outflow angle for line C for different rotational speed cases b) Outflow angle for line D for different rotational speed cases c) Outflow angle for line E for different rotational speed cases d) Outflow angle for stationary model for different outflow line cases

5.3 Fictitious forces

As explained in paragraph 4.4, fictitious forces need to be studied for describing well the flow in presence of rotation and for this reason they are presented in two different positions (upstream and downstream, precisely in the middle of the channel used for the study, points B and E of Figure 5.2) to get better idea of their behaviour. Coriolis force and centrifugal force are studied in this section. The centrifugal force – as understandable from paragraph 4.4 – follows a linear proportion with respect to the radius.

The plots present the values of Coriolis and centrifugal force moment according to the height of the blade, for different rotational velocity cases. The less constant variable is the Coriolis force computed along the line at the end of the channel (Figure 5.2 B). In that position, it is evident how the turbulence and the eddies are preponderant.

The radial velocity sign is influenced by the discontinuity of the wake hence, in the Figure 5.4 (b), results show a strong fluctuation that even increases with the enhancement of the rotational speed. Only in the case with rotational speed 25%, the Coriolis force changes sign just once, for all the rest of the simulations the variations occur more frequently.

In the highest omega case, the flow is pushed tangentially with momentum gaps that reach magnitudes greater than ten times the gap in the slowest rotational case, in the interval 0.7 ÷ 0.97 of $^{z}/_{h}$, where the most concentrated vortexes are.

Overall the Coriolis force keeps a negative value for the zones close to the tip and the hub, with a particular expansion for the second part. Everything is dependent of the direction of the velocity that is presented in the previous paragraph 5.2.

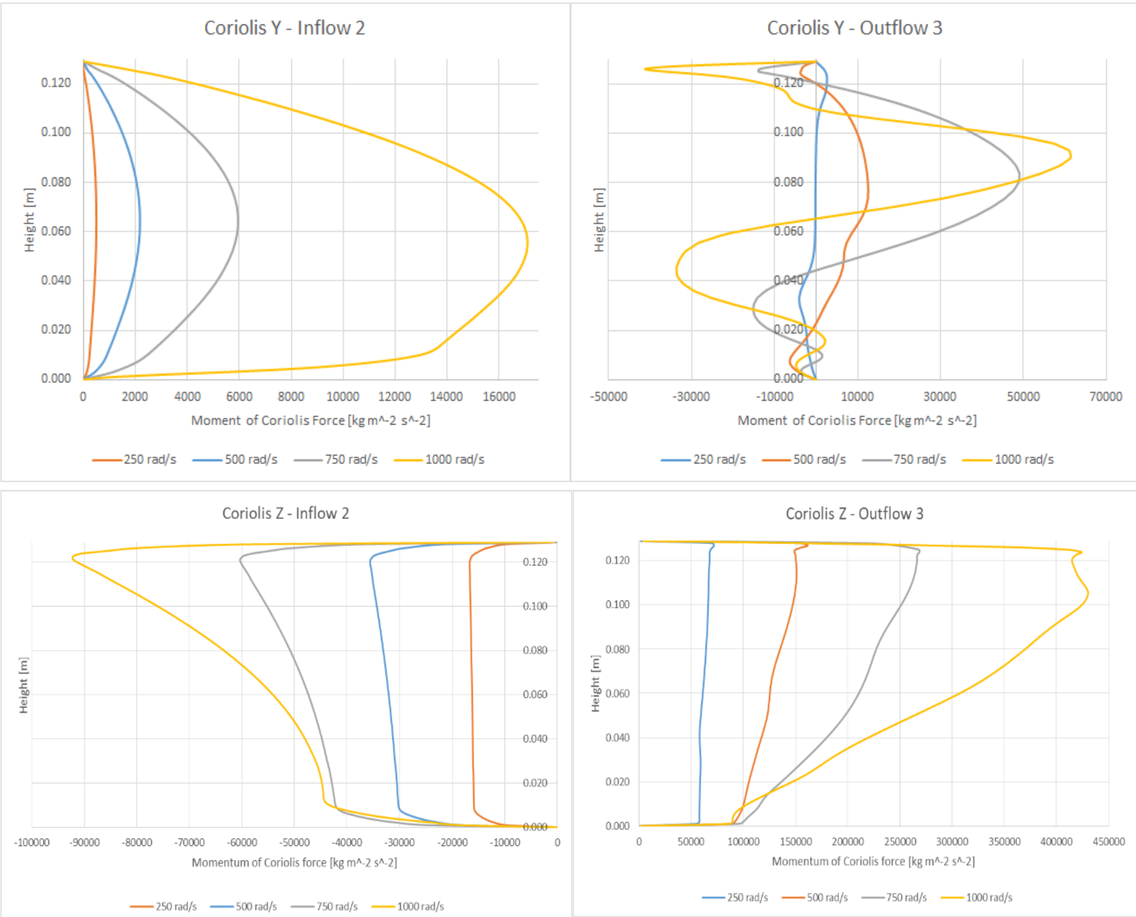

Figure 5.4 a) and b) Coriolis momentum along Y axis in lines B and E
c) and d) Coriolis momentum along Y axis in lines B and E

On the other hand, the Coriolis momentum analysed at the inflow presents only positive results due to constant behaviour of the radial velocity before meeting the airfoil. Also about the peaks, they keep a certain consistency showing themselves at mid span. These values increase considerably with the increase of rotational velocity, with an increment of more than 30 times between the fastest and slowest case.

Moreover, also the radial component of the Coriolis in Figure 5.4 (c) and (d) keeps a coherent trend linked to direction of the flow, upstream and downstream. In this case, the main property to be observed is the magnitude because, as written before, it is subtracted by the centrifugal force.

At upstream, the negative value gives a positive contribute to the centrifugal force, while downstream the radial Coriolis momentum reduces the power of the centrifugal force. The maximum values of momentum are visible at $z/h = 93\%$, in both plots; the only exception is represented by the radial Coriolis force at downstream for the 100% velocity case, where there are two relative peaks.

5.4 Pressure on the hub endwall

As written before, the prototype that is studied in this thesis is at the first step of its creation but the next upgrade wants to go deeper about thermodynamics and heat transfer. For future cooling studies, knowledge about this coefficient could be useful.
A dimensionless parameter $p^*_{endwall}$ is computed to show the different pressure distributions. Downwards, contours can be reviewed, from the lowest rotational speed to the highest (as usual during this study 0, 250, 500, 750, 1000 rad/s).
The variable is computed as ratio between the pressure of the point on the endwall $p_{x,endwall}$ and the value of pressure computed as mass flow averaged one at the plane at inlet of the studied channel $\bar{p}_{in}$.

$$p^*_{endwall} = \frac{p_{x,endwall}}{\bar{p}_{in}} \tag{5.1}$$

The contours of Figure 5.5 describe this factor according to the legend upwards and are related to the plane of lower wall.
The notable trend is a decrease of the overall pressure ratio coefficient with the increasing of the rotational speed: the coefficient gets values close to 1 in the stationary model while the other models have lower values. The flow is pushed to the blade tip: this arrangement gives a higher pressure to the tip and a lower one to the hub. In fact, the upstream of every contour presents higher values.
Pressure distribution provides also information about the presence of eddies, and in this particular case of corner vortex, as it is visible in Figure 5.5 (e), as point of minimum pressure coefficient. Constant trends are the greater values for the pressure side with respect to the suction side and a local peak close to trailing edge, while downstream pressure remains lower and almost homogenous.
Moreover the coefficient is more homogenous in case of higher rotational speed, because the quadratic dependency of centrifugal force by rotational speed pushes the air far from the hub. These results could be collected for giving a good knowledge for the heat transfer approach.

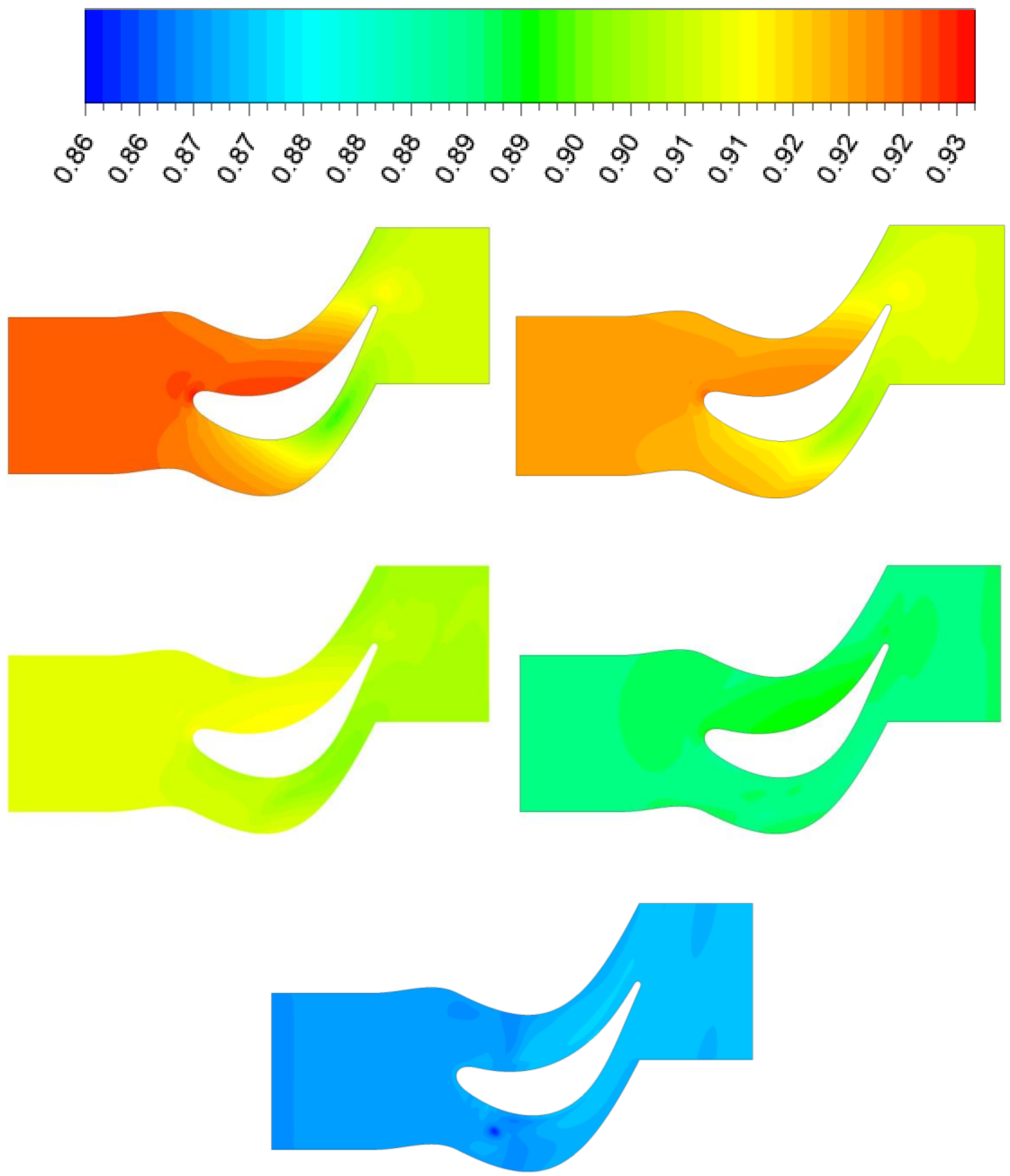

Figure 5.5 Relative pressure behaviour on the hub for different rotational speed cases (0, 250, 500, 750, 1000 rad/s)

5.5 Coriolis on centrifugal force ratio

Coriolis and centrifugal force change along the channel and their proportions swing following different conditions and rotational speeds. In particular, the case is studied in 4 different positions as planes orthogonal to the axial direction, describing leading edge, middle of the channel, trailing edge and downstream (Figure 5.6). The factor (1.3) is computed presented in paragraph 1.2 is now studied.

$$CC = \frac{\sqrt{(Cor_y^2 + Cor_z^2)}}{F_{centr}} \tag{1.3}$$

It wants to highlight the load and the importance of the two different forces in the entirety of the flow. This ratio was used some years ago (Bangga, et al., 2017) for studying the flow around the blade of a wind turbine, at different distances from the centre, while in a study from Politecnico di Milano an investigation about the relations between the Coriolis and centrifugal force is exposed (Persico, et al., 2015).

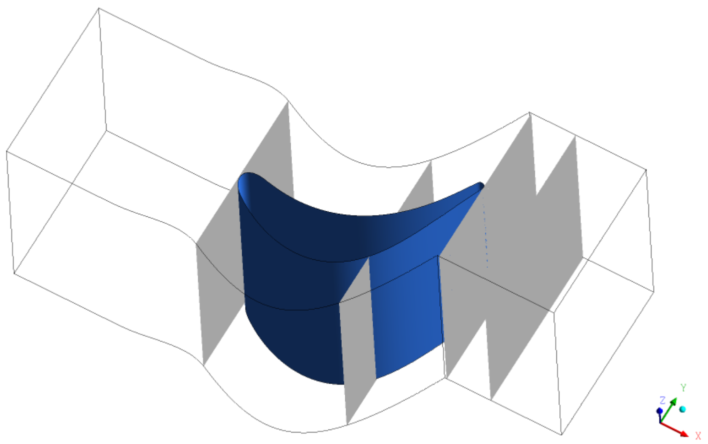

Figure 5.6 Planes used for the presentation of ratio CC

In this case instead the analysis is developed investigating 4 different rotational velocities: 25%, 50%, 75%, 100% (Figure 5.7). Legend is set different for each velocity case due to great range of values: with just a uniform legend the differences would be hardly appreciated. In general, at the same position, the ratio decreases with the increasing of the rotational velocity.

In the first plane, a double phase is ascertained and the position of leading edge is evident. In any case, the numerical value is almost everywhere lower than 1, also in the slowest case. In fact in this area, the components of velocity along radial and tangential direction – that influence the magnitude of Coriolis force – are not so preponderant due to the free stream. The gap of values is evident in the correspondence of the airfoil, with sudden reduction in the centre for the slowest cases and with smoother change for the other case.

In plane 2, instead, the important thing is the evidence of the difference between the pressure and suction side; indeed, in the left zone (suction), the flow has a higher velocity that makes Coriolis force increased.

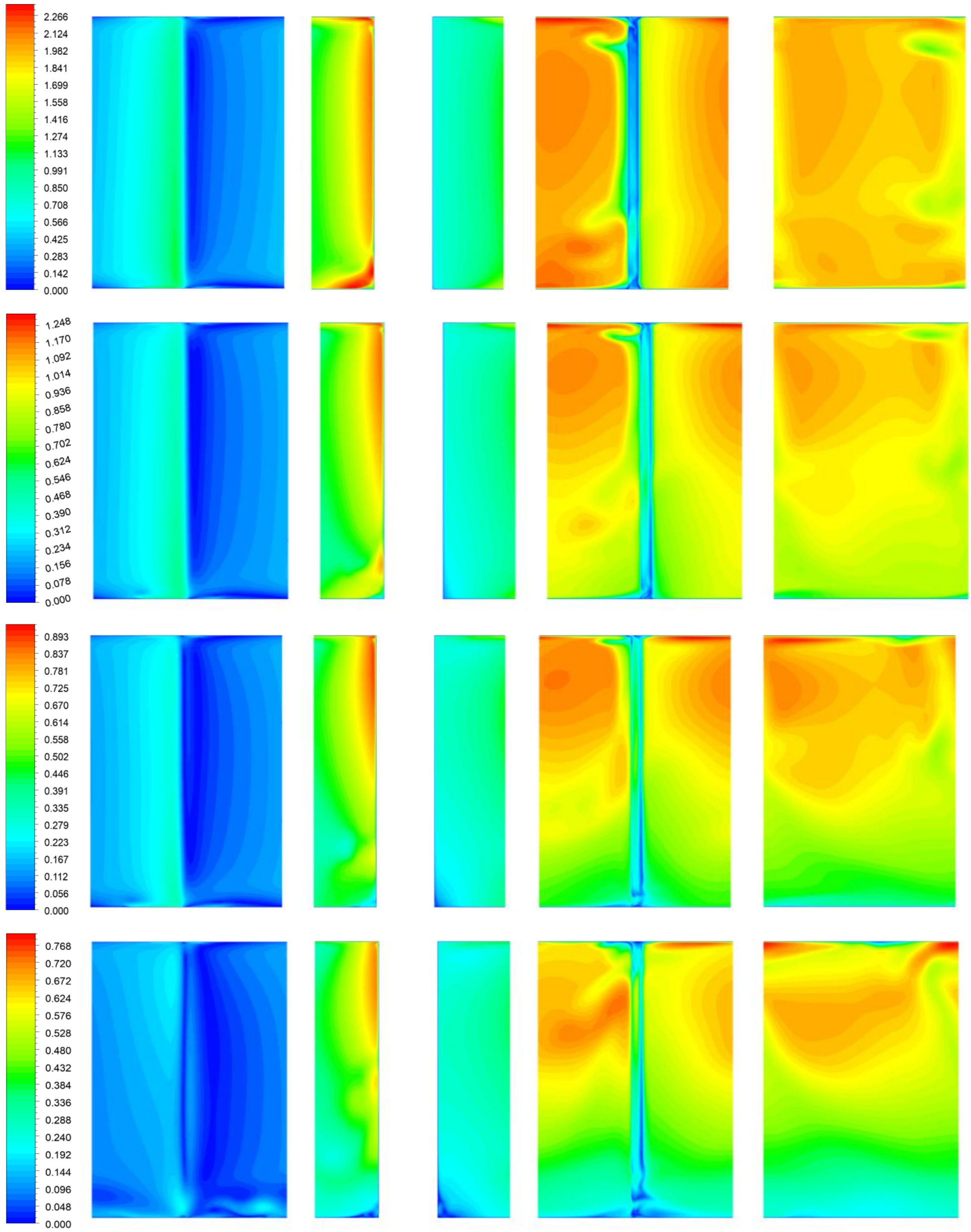

Figure 5.7 CC ratio showed on 4 different planes for 250, 500, 750, 1000 rad/s

Pressure side keeps a similar distribution for all the studied cases, while the suction side presents a different shape: it contains the maximum value but the hub part is subjected to a decrease of values with the increase of the rotational speed. A residue of symmetry is visible in 25% velocity case, at suction side. In the fastest cases, the passage vortex is seen close to the hub and in general the presence of secondary flow is visible.

The planes 3 and 4 present a ratio greater than one (25% and 50% velocity cases) due to presence of a consistent deviation of the flow that influences the Coriolis force quantity. In the first two simulations, also vortexes are detectable, while highest rotational velocity case presents lower values and more confused images. Plane 3 shows a net minimum zone close to the trailing edge marked by an expected reduction of the value. In the plane 4, the contribution of centrifugal force becomes greater in the upper part, with maximum values in the 100% case.

5.6 Vorticity analysis

Secondary flow is the consequence of the presence of the airfoil that interacts with the free stream flow and acts as turbulence generator: the obstacle creates velocity variation so generation of vortexes, as previously explained in paragraph 2.2.2. The main result is expressed by the analysis of eddies, vortex shedding and the vision of the streamlines.

The contours are obtained in the post processing by the representation of the variable of velocity curl or vorticity and are applied along the channel, perpendicular to the axial direction and the base. The 4 inspected planes differ from the previous paragraphs ones because interest about vorticity is concentrated in the last part of the airfoil and downstream; they are in positions of Figure 5.8. To have a better overview of the shapes and the magnitude, the legend limit is set at $200000\ \frac{1}{s}$, also if there are greater values but confined in little zones (more than a point only in plane 3 of the case with the 2 highest rotational speed), so they are considered negligible.

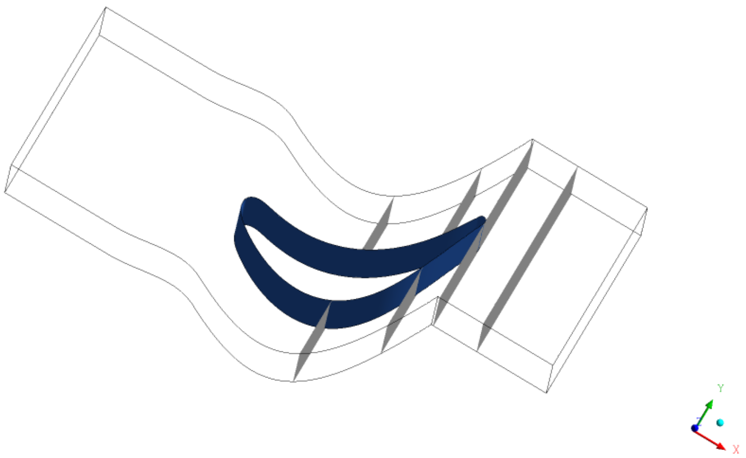

Figure 5.8 Planes used for the vorticity analysis

The first stripe of images describes the stationary case and we can notice the symmetry of the flow: no forces are applied and for approximation upper and lower boundaries are no slip walls. The 4 planes let to study the different steps of the flow and it is possible to notice the generation of the vortexes and their evolution; in particular, in the last contour, 3 eddies are seen and are more evident: passage vortex A, horse shoe vortex B, corner vortex C. From all of the secondary flow models presented by Ilieva (Ilieva, 2017) at paragraph 2.2.2., the study presented by research by University of Minnesota is adopted (Wang, et al., 1997).

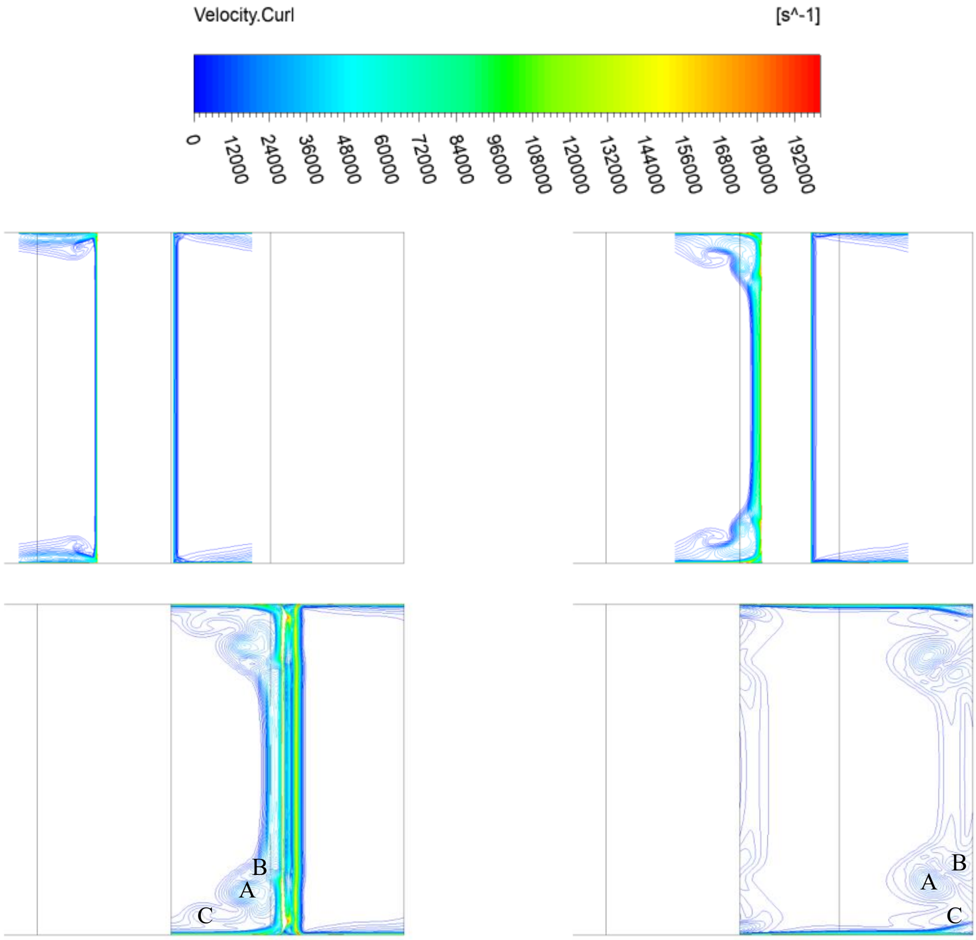

Figure 5.9 Vorticity along the 4 tested planes for the reference (stationary) case

In this section, the description of the results is going to be done. There is an overall high vortex power at the trailing edge that exceeds the legend limit. Increasing the rotational speed, the vortex profile loses the symmetry and, generally, the lower eddies are pushed upwards and the upper ones are squashed to the tip wall.

In Figure 5.10, plane 2 is presented for all the studied cases. A residue of symmetry is visible only in the slowest case. Passage vortex is clear in every frame, at 4% of the height of the blade for the 25% velocity case and 10 times higher for the fastest case. In the first two frames the presence of horse-shoe vortex is evident while in the last two corner vortex is visible above.

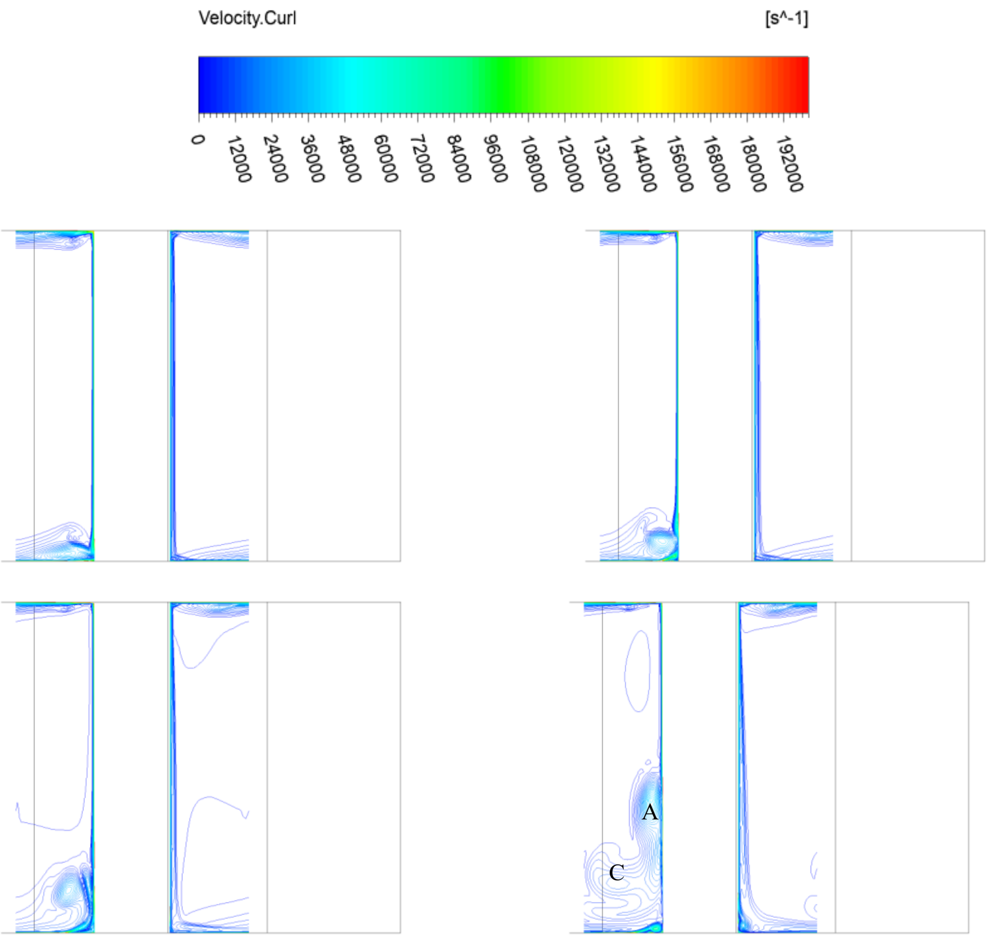

Figure 5.10 Vorticity for the plane 1 in case ω = [250, 500, 750, 1000] rad/s

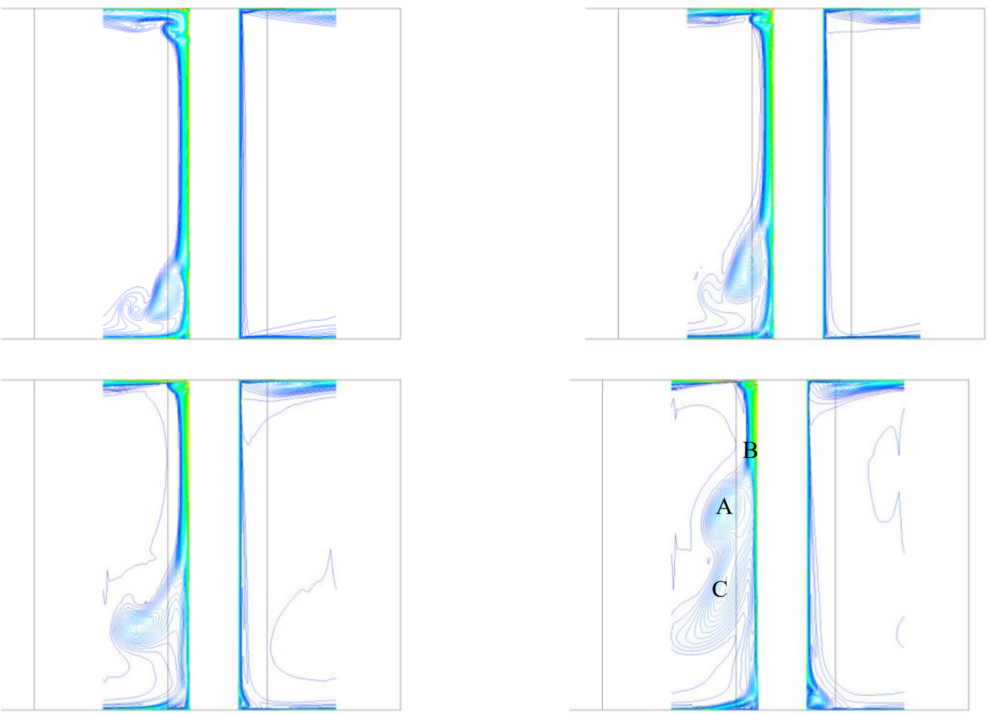

Figure 5.11 Vorticity for the plane 2 in case ω = [250, 500, 750, 1000] rad/s

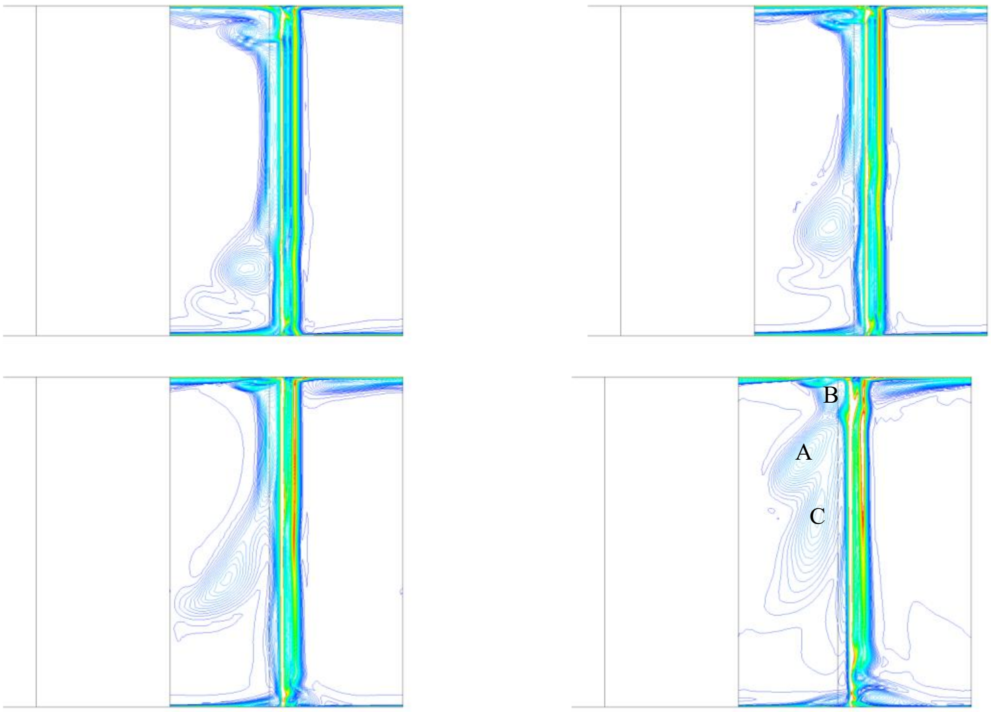

Figure 5.12 Vorticity for the plane 3 in case ω = [250, 500, 750, 1000] rad/s

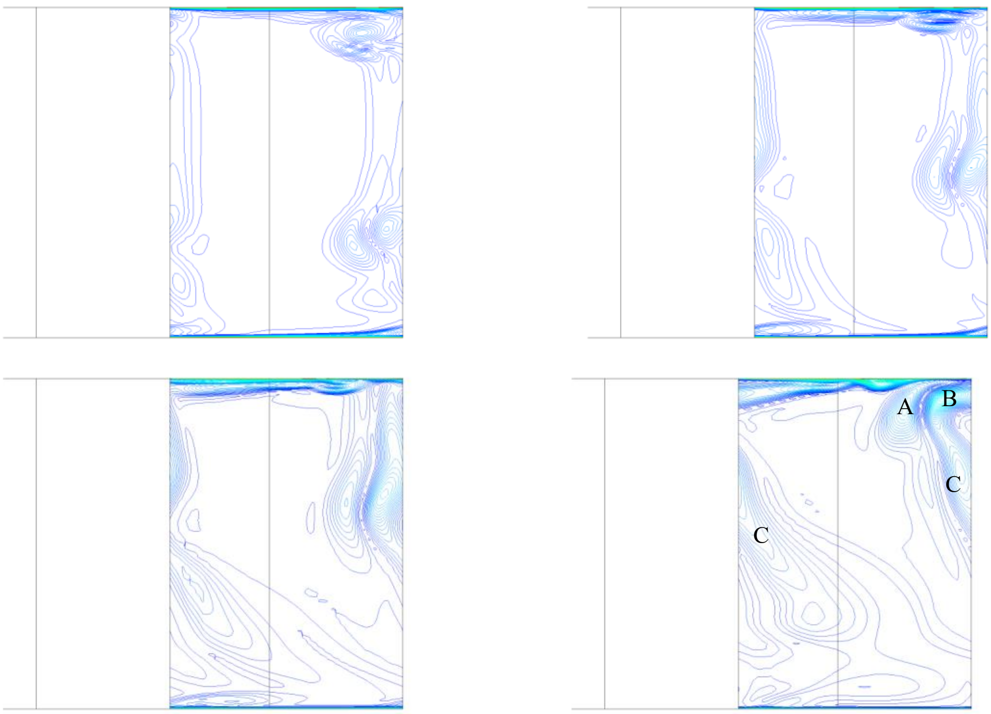

Figure 5.13 Vorticity for the plane 4 in case ω = [250, 500, 750, 1000] rad/s

In the Figure 5.11, the end part of the blade is described. Tip vortexes start to be more evident for the enhancement of value but they are flattened to the wall. Passage vortex continues to be evident in every frame, while corner vortex assumes more space for the 100% velocity case.

The horse-shoe vortex is hardly seen because is hidden in the vertical line, where the vorticity is really high. This part corresponds to the suction surface where the separation of flow occurs.

In the Figure 5.12, the conjunction of suction and pressure flow takes place, mixing the vortex shedding of the two parts. Tip vortexes are more evident in the slowest cases because they are not pushed to the upper wall as strongly as the ones of the 75% and 100% velocity cases. In the last frame the eddies move considerably to the upper part: the corner vortex is at $z/h = 60\%$, the passage vortex is at $z/h = 80\%$ and the horse-shoe vortex gets the 92% of the height of the blade. Moreover, a pressure side vortex is observed, close to the hub.

In last plane, a screenshot of the downstream situation is made. In the first image of the Figure 5.13 the eddies are well visible, while the consequent images show more confused behaviours. On the left, eddies coming from the other blade - due to periodicity – are detectable and in the fastest case they mix with the studied ones. At this time, vortexes are preponderant in the image but passage vortex and corner vortex are still distinguishable. Horse-shoe vortex, instead is really close to the passage one. In the tip, a high vorticity is generated by the flow and by the lower vortexes that press in that zone.

5.7 Loss pressure coefficient and SKE factor

Loss pressure coefficient is recalled from the paragraph 1.2 and it is analysed on 4 planes showed in Figure 5.14. The first plane wants to describe the leading edge behaviour while the other three planes are orthogonal to the stagger angle, so they follow the wake of the flow and for this reason they have got different width in the collection of contours of Figure 5.15.

$$C_{pt} = \frac{p_{t,in} - p_{t,x}}{\frac{1}{2}\rho U_{\infty}^2} \tag{1.1}$$

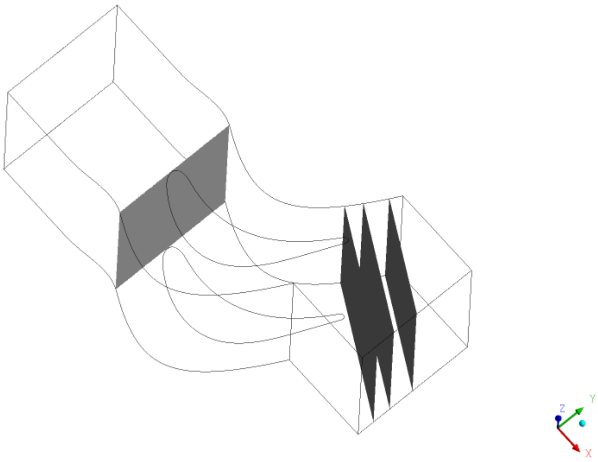

Figure 5.14 Planes for computation of loss pressure coefficient

In the Figure 5.15 we have some examples of this application, with the explanation of the tested planes and the relative legend, with a focus about the outlet flow.

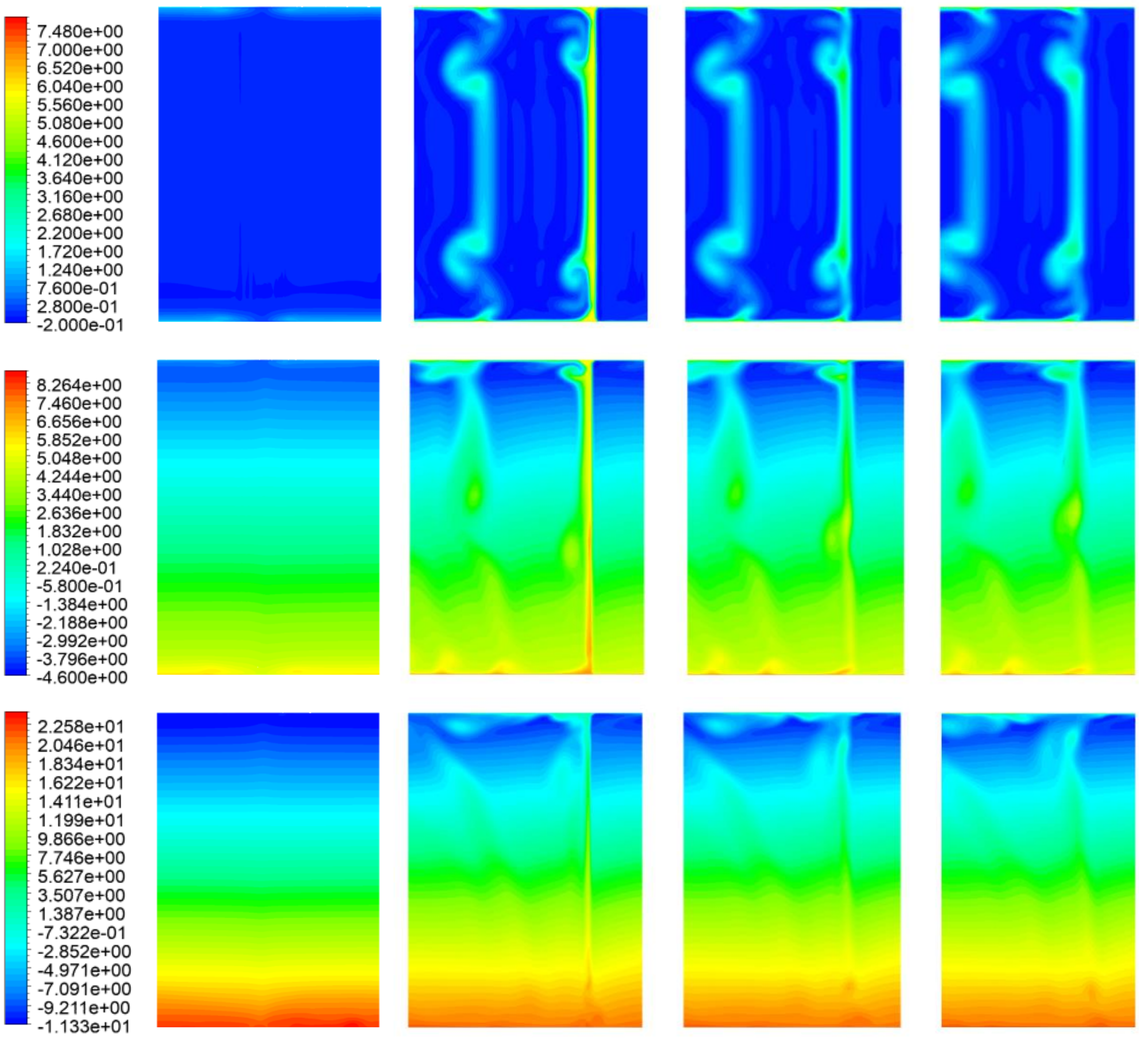

Figure 5.15 Loss pressure coefficient along 4 planes, for 0, 500, 1000 rad/s case

For 3 rotational velocity cases (0%, 50%, 100%), contours describe the behaviour of the non-dimensional coefficient on all the plane. As written before, the first plane shows the upstream distribution.
The range of values increases with the increase of rotational speed: in 100% velocity case the ratio gets values greater than 20 and lower than -10. In the stationary case, the range oscillates between -2 and 7.8.
Explaining about the first case (stationary case), a symmetric result is found again; the higher values areas show the lowest pressure measures - the difference is increased - and they are coincident with the vortex cores. The contours can also track the movement of the vortexes, which dissolve in the downstream planes. The maximum value is lower than 8 and does not represent a great zone (it is almost hidden in the vortex vertical profile).
The more evident peculiarity is the upstream contour, which is homogenous for stationary case while presents a progressive trend, with higher values close to the hub.
For the second stripe, the position of the maximum value area is at the same of the stationary case, but the down part is confused by values close to zero. The relative maximum moves from $z/h = 40\%$ to $z/h = 50\%$ between plane 2 and plane 4, while some absolute maximum values are adjacent to lower wall.
The stripe about 100% rotational velocity case shows how the behaviour is similar for all the planes: a high values zone is close to the hub, while in tip zone some vortex shedding breaks the stratification.
This factor can be useful for eventual validation because it is easier revealing pressure measurements in a test rig and then comparing with simulation.
Quoting again the paragraph 1.2, the Second kinetic energy factor is recalled:

$$C_{SKE} = \frac{v^2 + w^2}{U_\infty^2} \tag{1.2}$$

The factor is used to analyse part of second half of the channel, from the middle of the airfoil to the trailing edge. Coefficient is computed through planes that are orthogonal to the camber line and describes the flow before the outlet phase, as in Figure 5.16. High values symbolize a relevant turbulence activity: v and w are the factors that produce effective flow deviation. As before in this paragraph, 3 rotational velocity cases are analysed (0%, 50%, 100%) in Figure 5.17.
For the stationary case, the symmetry is conserved. In the first plane the distinction between suction and pressure side is net; in the first one C_{SKE} gets the maximum value close to the tip, with magnitude of about 7, while an high values zone is present in all the area. The pressure side instead shows a contour with preponderance of U_∞^2 with ratio smaller than 1.

In the subsequent planes, this strong difference diminishes. Some relative minimum peaks are seen in the vortex cores.

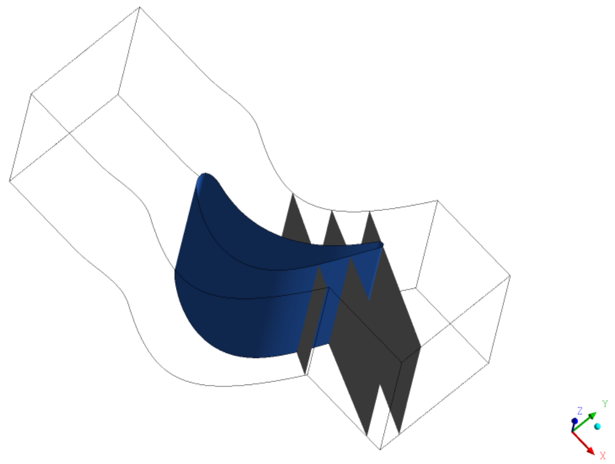

Figure 5.16 Planes for computation of second kinetic energy factor

In the 50% velocity case, the factor gets higher values close to 10. In plane 1, some differences and some analogies can be found with respect to stationary case: the suction side, losing its symmetry, shows high C_{SKE} for the upper side that decreases gradually downwards, until getting almost null result. At the same time, pressure side is very similar to the precedent case. In planes 2 and 3, the results show a decrease that goes upwards for the suction side while the pressure side increases its values. In plane 2, the tip presents again an high value due to the centrifugal force and the deviation caused by vorticity.
For the 100% velocity case, a growth of the factor is evident. Moreover, contours of planes 2 and 3 show clearly spots close to the tip where C_{SKE} goes to 15. This increment is made more evident by the lower region that is characterized by values close to 0, more than the previous cases. In addition, the effect of rotational velocity is clear because the relative minimum area – which is almost vertical in previous planes – has got now a sloped shape.

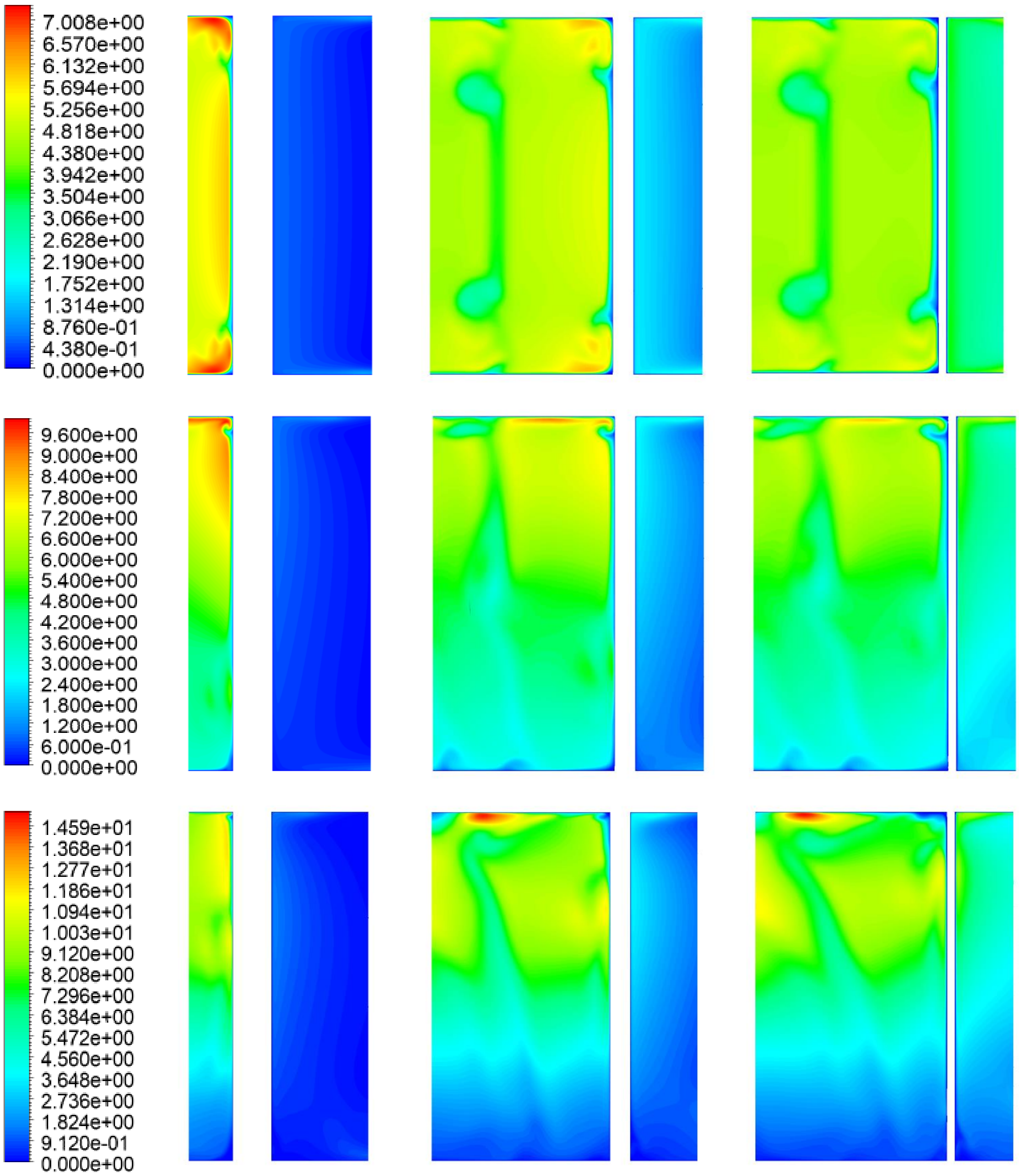

Figure 5.17 Second kinetic energy factor along 3 planes (upper figure), for 0, 500, 1000 rad/s case

5.8 Plausibility

This section provides an examination of the reality of the results and the values. Validation is a concept that cannot be utilized in this work, because a real experiment is not performed to check – and so to validate – the results of the simulation. The possible discussion is about the plausibility of the numerical outcomes.

A similar physical approach was designed in the case of study about effects of simulated rotation on tip leakage in a planar cascade (Yaras & Sjolander, 1992) and already presented

in paragraph 1.2. Scientists exploited the experimental rig designed by Danias (Danias, 1987) to collect data about the rotation effects, both aerodynamics and thermal ones. A conveyor belt reproduces the revolving effects also if the planar configuration does not allow theoretically and perfectly. In the second part of the paper (Yaras, et al., 1992), contours of non-dimensional streamwise vorticity are presented and give a good hint to this thesis; being the thermal process the main point of the scientific investigation, all results taken from simulations cannot be compared because of aerodynamic subject.
The similarity can be easily found in classical annular cases where the vortexes are affected by the rotational forces, as reported by the experiments executed by Turbomachinery Laboratory of Swiss Federal Institute of Technology (Schlienger, et al., 2005) (Porreca, et al., 2007). Correlation is present partially also in studies about cascades where rotation is not applied, but where the symmetric behaviour is clear; Korea University (Moon & Koh, 2000) and University of Brescia (Perdichizzi, 1990) published important results.

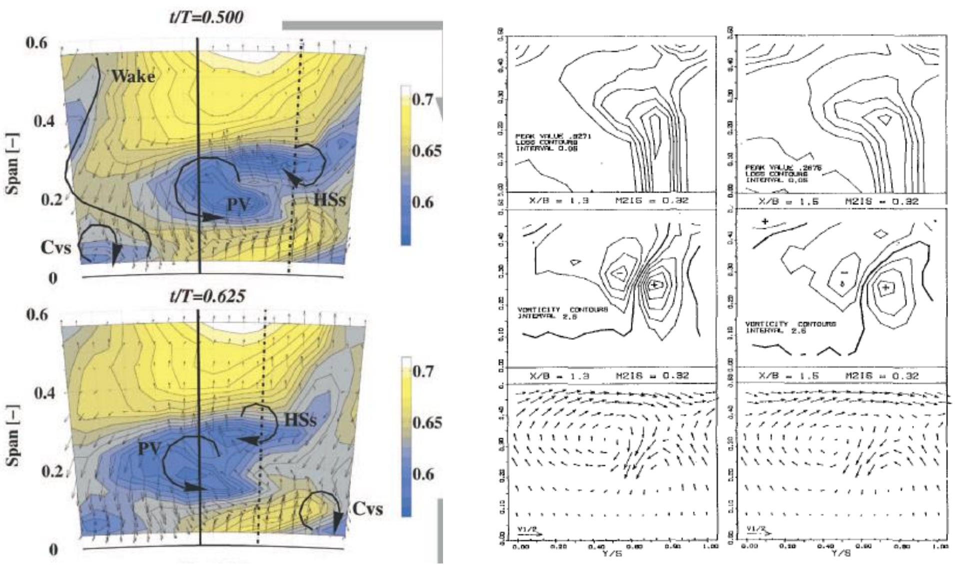

Figure 5.18 Contours reported by scientific papers a) Schlienger, et al., 2005 b) Perdichizzi, 1990

In conclusion, validation is not possible, while the study is plausible because the results follow physics rules and it tries to adapt them to an unconventional configuration. Nevertheless, it is fitting to remind that data are affected by an approximation since the whole work is based on an important premise explained at paragraph 4.4.

6 Conclusions

The goal of the thesis is the investigation of the influence of rotation on aerodynamics in axial turbine cascades and the eventual negligibility of the rotational speed on these parameters; several points have been discussed. After the presentation of fundamentals, the model and the results, some conclusions are declared.

Rotational velocity influences the pressure of the flow. In particular the pressure around the airfoil increases with the enhancement of ω value and for extreme working conditions some adverse pressure zones are measured. For the hub wall, instead, pressure at the base decreases if rotational velocity increases. The value is always greater at upstream and at pressure side; from 0% to 100% of rotation, the reduction of pressure gets the 7%.

Direction of flow is considerably conditioned by rotation, mostly at outflow. The magnitude of deviation grows if the rotation intensifies. Changes of direction can get ±30 degrees, both in zones that follow the outflow wake – so more influenced by vortex shedding – and in zones far from the projection of stagger angle. The difference is that in the second one the deviation keeps for more along the height while in the other one is almost punctual.

Distribution of Coriolis and centrifugal force is similarly scaled on the studied planes, independently from the rotation. This quantity instead affects the values of the forces: Coriolis force is bigger and affects more the flow when lower rotational speeds are involved.

Effects on vorticity are sufficiently evident. Figures of contours show how the increase of rotational speed generates stronger vortexes. The rotation moves the eddies up, in fact in the 100% rotational speed passage and corner vortexes occupy a big part of the area just at middle of airfoil. For strong rotations, the vorticity gets the maximum value and vortexes move upwards, requiring attention for the working conditions.

As explained in paragraph 5.8, the validation of the study is not possible due to non-existence of an experimental test rig where the rotation can be applied. The results are judged plausible thanks to previous experimental data found in scientific literature.

The presented work is not enough to evaluate the negligibility of some parameters from the original prototype. In particular, it is showed that rotation (especially values that bring flow close to supersonic condition) influences several outcomes. Reducing the physical study to a stationary non-rotating test rig is not reccomended as successful approach, because many aspects are not considered while rotational speed – and its forces – covers all of them.

Unluckily the study is not sufficient for giving precise answers to the proposals of investigation set at the beginning. More studies will have to be held to show a more accurate picture of the phenomenom, starting from the qualtative and quantitative hints of this thesis.

6.1 Outlook

Some suggestions are given now for continuing this study and especially for analyzing it deeper.

A good purpose for the future could be the adaptation of the prototype to an annular configuration for applying the revolving effect and studying the effects, according to the approach of paragraph 4.4. This kind of application could be very expensive but a simulation or an experimental test rig could confirm or deny the results that are collected in this work.

Another investigation could go through the different parameters that influence the aerodynamics behavior of the flow. The main effort was reserved to the rotational speed but other factors as temperature, pressure and pressure gap could be taken as reference; interesting variables could be exploited just searching in the scientific literature. An example is provided by the influence of the load distribution on secondary flow (Weiss & Fottner, 1995) or by the Mach number (Perdichizzi, 1990).

Beyond the aerodynamics and secondary flow aspect, this thesis could be a good overview for running a study about the thermal and heat transfer part of the turbine cascade. The application of the cavities under the base of the cascade could replace the usual cooling arrangement, so they could better complete the dissertation. Linked to the thesis, several scientific papers can introduce this topic due to the big impact that gives on the efficiency and energetic features of turbomachinery elements.

The effects of rotation on a gas turbine blade internal cooling system were studied by University of Florence (Massini, et al., 2017) and by School of Energy Science and Engineering (Aihua, et al., 2019). To go more in detail, other collateral effects are faced, as the effect of Coriolis and centrifugal force in 2006 (Sleiti & Kapat, 2006) or thermo-mechanical modeling of high pressure turbine (Brandao, et al., 2016).

7 Acknowledgements

Prof. Daniela Anna Misul and Prof. Daniele Salvadori from Politecnico di Torino are gratefully acknowledged.
M. Sc. Marco Hahn supported and followed this report work: particular gratitude is given to him for the proposal of the work.
This study has been possible also thanks to Erasmus Plus Program, that allowed the permanence and the experience at Karlsruher Institut für Technologie and at Institut für Thermische Strömungsmaschinen.

References

Aihua, D. et al., 2019. *Rotation Effect on Flow and Heat Transfer for High-Temperature Rotor Blade in a Heavy Gas Turbine.* Harbin: Springer Nature.

ANSYS, Inc., 2009. *ANSYS CFX-Solver Theory Guide.* Canonsburg, PA 15317: s.n.

Aqilah, F. et al., 2018. *Study of mesh quality improvement for CFD analysis of an airfoil.* Department of Mechanical and Production Engineering, Ahsanullah University of Science and Technology, Dhaka: s.n.

Ariff, M., Salim, S. M. & Cheah, S. C., 2009. *Wall Y+ approach for dealing with turbulent flow over a surface mounted cube: part 1 – low Reynlds number.* University of Nottingham (Malaysia Campus), Semenyih, 43500, Selangor, MALAYSIA: s.n.

Aunapu, N. V., Volino, R. J., Flack, K. A. & Stoddard, R. M., 2000. *Secondary Flow Measurements in a Turbine Passage With Endwall Flow Modification.* United States Naval Academy: Journal of Turbomachinery.

Bangga, G. et al., 2017. *Investigations of the inflow turbulence effect of rotational augmentation by means of CFD.* University of Stuttgart: s.n.

Bradshaw, P., 1996. *Turbulence modeling with application to turbomachinery.* Stanford University, CA: s.n.

Brandao, P., Infante, V. & Deus, A., 2016. Thermo-mechanical modeling of a high pressure turbine blade of an airplane gas turbine engine. *Science Direct,* Issue XV, pp. 190-196.

Chaluvadi, V. S. P. et al., 2001. *Blade-Row Interaction in a High-Pressure Turbine.* University of Cambridge: Journal of Propulsion and Power.

Danias, G., 1987. *Contributions to the study of tip leakage flow in a planar cascade of turbine blades.* Ottawa: s.n.

Davidson, D. L., 2002. *The Role of Computational Fluid Dynamics in Process Industries.* Washington: NATIONAL ACADEMY OF ENGINEERING.

Eckerle, W. A. & Awad, J. K., 1991. Effect of freestream velocity on the three-dimensional separated flow region n front of cylinder. *ASME Journal of Fluids Engineering,* Issue 113, pp. 37-44.

Epifanov, V. M., 2011. *BOUNDARY LAYER.* s.l.:s.n.

European Commission, 2021. *Pathway to a Healthy Planet for All.* Brussels: s.n.

Ferziger, J. H., 2002. *Computational methods for fluid dynamics.* 3. ed. s.l.:s.n.

Hawthorne, W. R., 1967. *Fluid Mechanics of Internal Flow.* Amsterdam: Elsevier.

Horlock, J. H. & Lakshminarayana, B., 1973. *Secondary flows: theory, experiment and application in turbomachinery aerodynamics.* Cambridge: s.n.

Ilieva, G., 2017. *A Deep Insight to Secondary Flows.* Technical University – Varna, Bulgaria: s.n.

Keller, H. B., 1978. *NUMERICAL METHODS IN BOUNDARY-LAYER THEORY.* Applied Mathematics, California Institute of Technology, Pasadena, California 91 125: Annual Reviews Inc..

Lampart, P., 2009. *Investigation of endwall flows and losses in axial turbines. Part I. Formation of endwall flows and losses.* Warsaw: Journal of theoretical and applied mechanics.

Langston, L. S., 2001. *Secondary flow in axiala turbines - A review.* Storrs: New York Academy of Sciences.

Li, Y. & Zheng, Q., 2006. *Numerical simulation of a multistage radial inflow turbine.* Harbin Engineering University: s.n.

Lyczkowski, R. W., 2010. *The History of Multiphase Computational Fluid Dynamics.* Argonne, Illinois: American Chemical Society.

Massini, D. et al., 2017. *Effect of Rotation on a Gas Turbine Blade Internal Cooling System: Experimental Investigation.* Florence: Journal of Engineering for Gas Turbines and Power.

Moon, Y. J. & Koh, S., 2000. *Counter-rotating streamwise vortex formation in the turbine cascade with endwall fence.* Seoul: Pergamon.

Pattanayak, L., 2015. *Thermodynamic modeling and Exergy Analysis of Gas Turbine Cycle for Different Boundary conditions.* Noida: International Journal of Power Electronics and Drive Systems.

Perdichizzi, A., 1990. *Mach number effects on secondary flow development downstream of a turbine cascade.* University of Brescia: Journal of Turbomachinery.

Persico, G., Pini, M., Dossena, V. & Gaetani, P., 2015. *Aerodynamics of Centrifigal turbine cascades.* Milano & Delft: Journal of Engineering for Gas Turbines and Power.

Physics, D. o., 2020. *Coriolis and Centrifugal Forces.* Brock Univesity, Canada: s.n.

Pope, S. B., 2000. *Turbulent Flows.* Cornell University: s.n.

Porreca, L., Hollenstein, M., Kalfas, A. I. & Abhari, R. S., 2007. *Turbulence Measurements and Analysis in a Multistage Axial Turbine.* Swiss Federal Institute of Technology, 8092 Zürich, Switzerland: JOURNAL OF PROPULSION AND POWER.

Qi, N., Wang, H., Zhang, K. & Zhang, H., 2010. *Numerical simulation of fluid dynamics in the stirred tank by the SSG Reynolds Stress Model.* Beijing & Adelaide: Higher Education Press and Springer-Verlag Berlin Heidelberg.

Schlichting, H. & Gersten, K., 2017. *Boundary-Layer Theory.* 9. ed. Braunschweig & Bochum: Springer.

Schlienger, J., Kalfas, A. I. & Abhari, R. S., 2005. *Vortex-wake-blade interaction in a shrouded axial turbine.* Zurich: Journal of Turbomachinery.

Simpson, R. L., 1989. *Turbulent boundary layer separation.* Blacksburg, Virginia: Annual Reviews Inc..

Sleiti, A. & Kapat, J. S., 2006. *Effect of Coriolis and Centrifugal Forces at High Rotation and Density Ratios.* Orlando: JOURNAL OF THERMOPHYSICS AND HEAT TRANSFER.

Townsend, A. A., 1950. *The structure of the turbulent boundary layer.* Cambridge: s.n.

Wang, H. P., Olson, S. J., Goldstein, R. J. & Eckert, E. R. G., 1997. *Flow Visualization in a Linear Turbine Cascade of High Performance Turbine Blades.* University of Minnesota: s.n.

Weiss, A. P. & Fottner, L., 1995. *The influence of load distribution on secondary flow in straight turbine cascades.* Universitat der Bundeswehr Munchen: Journal of Turbomachinery.

Yaras, M. I. & Sjolander, S. A., 1992. *Effects of simulated rotation on tip leakage in a planar cascade of turbine blades: Part I - Tip gap flow.* Ottawa: Journal of Turbomachinery.

Yaras, M. I., Sjolander, S. A. & Kind, R. J., 1992. *Effects of simulated rotation on tip leakage in a planar cascade of turbine blades: Part II - Downstream flow field and blade loading.* Ottawa: s.n.